nature geoscience

SUPPLEMENTARY INFORMATION

https://doi.org/10.1038/s41561-018-0199-0

In the format provided by the authors and unedited.

High temperatures in the terrestrial mid-latitudes during the early Palaeogene

B. D. A. Naafs[1]*, M. Rohrssen[1,2], G. N. Inglis[1], O. Lähteenoja[3], S. J. Feakins[4], M. E. Collinson[5], E. M. Kennedy[6], P. K. Singh[7], M. P. Singh[7], D. J. Lunt[8] and R. D. Pancost[1]

[1]Organic Geochemistry Unit, School of Chemistry, School of Earth Sciences, and Cabot Institute, University of Bristol, Bristol, UK. [2]Department of Earth and Atmospheric Sciences, Central Michigan University, Mount Pleasant, MI, USA. [3]School of Life Sciences, Arizona State University, Tempe, AZ, USA. [4]Department of Earth Sciences, University of Southern California, Los Angeles, CA, USA. [5]Department of Earth Sciences, Royal Holloway University of London, Egham, UK. [6]Department of Paleontology, GNS Science, Lower Hutt, New Zealand. [7]Coal and Organic Petrology Lab, Department of Geology, Banaras Hindu University, Varanasi, Uttar Pradesh, India. [8]School of Geographical Sciences and Cabot Institute, University of Bristol, Bristol, UK.
*e-mail: david.naafs@bristol.ac.uk

Supplementary information to *High temperatures in the terrestrial mid-latitudes during the early Paleogene* by Naafs et al.

1. Description of lignites and age models

1.1 Schöningen lignite (Germany)

36 samples were collected from Seam 1 in the Schöningen Südfeld mine, northern Germany (51.13°N, 11.00°E) (Fig. S1). Samples no. 33 to 1 were obtained from the high-resolution sampling series of 2008 and 2012[S1,2]. Samples XXIII 4a to XXXIII7b were obtained from subsequent low-resolution sampling[S2]. The lignites in this mine were deposited as peat in a low lying coastal setting[S3] with a paleolatitude of around 46 °N. The seam from which the samples are derived is ~2.7 m thick and is overlain and underlain by brackish to shallow marine, clastic sedimentary deposits[S3,4].

The dinocyst zone D 5nb was recognized above the Main Seam in the nearby Emmerstedt area by Ahrendt et al.[S5]. If the Main seam is coeval at both sites this would indicate that Seam 1 at Schöningen is earliest Eocene. However, within marine Interbed 2, directly above Seam 1, there is a dramatic increase in the abundance of the dinocyst *Apectodinium*[S3] which may represent the onset of the Paleocene-Eocene Thermal Maximum (PETM) as it does at other sites[S6,7]. However, none of the studied samples yielded a negative $\delta^{13}C$ excursion that would suggest it was deposited during the main body of the PETM[S4]. Therefore, Seam 1 is considered to be either very latest Paleocene or very earliest Eocene in age. During the subsequent early Eocene (Seam 3 upwards), there is a long-term temperature maximum recorded from both the lignites and nearshore marine interbeds, consistent with changes in the palynological assemblage[S2,3]. As this interval may include the Early Eocene Climatic Optimum (EECO)[S1], this suggests that Seam 1 was deposisted prior to the EECO. Further details of sample positions and the lignite sequence at Schöningen can be found in the supplementary material to Robson et al.[S1] and Inglis et al.[S2].

1.2 Cobham lignite (UK)

A total of 7 samples were used from the Cobham Lignite Bed at Cobham, UK (51.40°N, 0.40°E). Samples were obtained from previous sampling events[S8]. This lignite was deposited in a low-lying freshwater setting at the southwest shore (very near sea-level) of the North Sea (~48 °N palaeolatitude)[S9,10]. The Cobham Lignite Bed

at Cobham comprises a thin clay layer (<3 cm) at the base, overlain by a laminated lignite (~55 cm thick). This is succeeded by another thin clay layer (<10 cm) and overlain by a blocky lignite (~130 cm).

The Cobham Lignite Bed at Cobham is underlain by the Upnor Formation, which, at a nearby site, is dated as latest Palaeocene by means of the occurrence of calcareous nannoplankton zone NP9 and magnetochron C25n in its lower part[S10]. The shallow-marine Woolwich Formation, which overlies the Cobham Lignite Bed at Cobham, contains the *Apectodinum* acme indicating that it is within the PETM[S9,10]. In addition, at Cobham a negative carbon isotope excursion (CIE) of ~ 1 ‰ is present near the top of the laminated lignite (54.4-55.3 cm) slightly below the middle clay layer, interpreted as being the negative CIE characteristic of the PETM[S8-10]. Here we used 7 samples from the lower laminated lignite below the inferred PETM CIE and thus of very latest Paleocene age.

1.3 Indian lignites

Lignites were collected from mines in several sites in the Rajasthan and Gujarat regions of western India (0-5 °N palaeolatitude). Paleogene-age subbituminous coals from the Meghalaya, Assam, and Nagaland regions of northeastern India were also analysed, but these lignites lacked GDGTs due to higher thermal maturity. All of these sections are associated with over- and/or underlying marine sediments, a characteristic consistent with deposition along the coastal margins of India[S11-15]. The elemental composition (relative concentration of C, H, O, N, and S) and TOC (total organic carbon) of the organic matter of Rajasthan and Gujarat lignites, in general, are suggestive of forest vegetation as the main source and peatification under topogenous conditions. This is further supported by the study of paleomires using petrography based information, using macerals as tools, which indicate deposition under tropical humid climatic conditions at a coastal setting with intermittent fluvial incursions[S16-18].

Several lignites from the Kachchh Basin were analysed: one sample from the Matanomadh seam (present-day lat./long.: 23°30’05”N, 68°58’E) and two samples from the Panandhro seam (present lat./long.: 23°41’34”N, 68°46’24”E). The Naredi Formation, including these lignite seams, is largely constrained to the early to early middle Eocene on the basis of the age diagnostic foraminifera and pollen[S11,19,20]. Abundant dinoflagellate cysts in associated shales and mudstones and pollen

dominated by mangrove (*Nypa*) imply an occasional marine influence in a near-shore environment[S20].

In addition, 3 lignite samples from the Khadsaliya Clays of the Saurashtra Basin (present lat./long. 21°39'32"N, 72°12'08"E) were analysed. These lignites are considered early Eocene on the basis of pollen and fungal remains[S21,22]. The Khadsaliya Clays comprise gray to greenish-gray clays, carbonaceous clay, and lignite deposited in a woody swamp[S23].

Lastly, 3 lignite samples from the Palana Formation lignites were analyzed; one from the Barsingsar seam, Bikaner basin (present lat./long. 27.84°01N, 73.20°04E); and two from Kasnau Matasukh seam, Nagaur Basin (present lat./long.: 27°06'25"N, 74°04'30"E). The age of the Palana Formation is not well constrained. The Palana Formation was initially assigned to the Eocene on the basis of correlation with lignites in Pakistan[S24] and broad age constraints derived from pollen[S25,26]. However, planktonic foraminifera in the overlying Marh Formation have been suggested to be of late Paleocene-early Eocene age[S27,28]. In addition, the more recently described osteoglossid and lepisosteid fish are consistent with a Paleocene age for the Palana Formation[S29]. As such the Palana Formation is considered of late Paleocene age.

1.4 Otaio River section lignites (New Zealand)

The Paleocene to Eocene Broken River Formation overlain by the early Eocene Kauru Formation is exposed in the Otaio River section, near Otaio Gorge, eastern South Island, New Zealand. The Broken River Formation exposures include two lignite seams >1 m thick and several thinner lignite seams[S30]. Palynological analyses[S31] and unpublished data indicate that the lower portion of the Otaio River section spans the PETM and the rest of the Broken River Formation exposed in the Otaio River section belongs to the New Zealand stages Waipawan to Mangaorapan (56.0 Ma to 48.9 Ma)[S32]. In order to avoid possible overlap with the PETM, we used samples from only the upper lignites, i.e. early Eocene. The 6 samples analysed were taken from thin lignites separated by dark brown sandstones as well as from the c. 2m thick seam at the top of the Broken River Formation exposure in Otaio River. Palynological analyses indicate that the samples fall into the NZ MH1 pollen zone, except for the lowermost sample analysed here (OGp30) which is placed in the PM3b pollen zone.

2. Detection of *iso*GDGT-5 and -6 in peats and lignites

*Iso*GDGT-5 and -6 were identified based on 1) comparison of relative retention times (Fig. S2 and S3) with published data[S33], 2) comparison of LC-MS chromatograms with those of a sample from Champagne pool, a thermal hot spring with a temperature of 75 °C and pH of 5.5 that contains *iso*GDGT-0 to -8[S34], and an acid-hydrolysed extract of the extremophile *Thermoplasma acidophilum* (Matreya, catalog # 1303) (Fig. S4), which is known to produce *iso*GDGT-0 to -6, but not crenarchaeol[S35], and 3) co-injection of a peat sample from Peru and the acid-hydrolysed extract of the extremophile *T. acidophilum* (Fig. S5).

3. Environmental controls on the *iso*GDGT distribution in modern peat

Decades of research, based on both culture experiments and natural archives such as marine sediments and thermal hot springs, have demonstrated that Archaea can alter the distribution of their *iso*GDGT membrane-spanning lipids in response to changes in environmental parameters such as temperature and pH[S36-42]. However, so far it is unknown whether the *iso*GDGT distribution in terrestrial settings such as peats varies according to environmental parameters. Below, we discuss the *iso*GDGT distribution in a wide range of modern peats to assess whether key-environmental parameters such as peat pH and mean air annual temperature have an impact on the *iso*GDGT pool in peats. The peat samples were obtained from a database as described in detail in Naafs et al.[S43,44]. In short, we analyzed >470 samples from 96 different peatlands from around the world for their GDGT distribution. The database consists of peats from a wide range of environments with a total span in mean annual air temperature (MAAT) from -8 to 27 °C and pH range from 3 to 8. pH data does not exist for all peats and *iso*GDGTs were below detection limit in a number of peat samples (predominantly in samples from the very top of peat).

3.1 pH dependence

In thermal hot springs, where *iso*GDGTs are produced by extremophiles, the *iso*GDGT distribution is influenced by environmental factors such as pH, with increasing cyclisation at lower pH and higher temperatures[S34,41,45]. It is largely unknown whether the *iso*GDGT distribution in mesophilic (terrestrial) settings is influenced by pH, although Xie et al.[S46] recently demonstrated that the *iso*GDGT

distributions of a number of Chinese and American mineral soils as well as enrichments of terrestrial *Thaumarchaeota* grown over a narrow pH range (6.5 to 8) were correlated with pH.

We found no significant correlation (R^2<0.2) between the relative abundance of individual *iso*GDGTs with cyclopentane rings (both if crenarchaeol was included and when not) and pH (Fig. S6). The only *iso*GDGT that had a clear correlation (R^2=0.56) with pH was *iso*GDGT-5.

We collected a range of samples from peatlands in the Peruvian Amazon. These tropical peats (MAAT ~26 °C) are located less than 200 km apart, but span a pH range from 6.1 to 3.8. The peats with pH < 5.1 contain *iso*GDGT-5, whereas those with a pH > 5.1 do not (Fig. 2 of main manuscript). To explore this further, we compared the relative abundance of *iso*GDGT-5 relative to the other *iso*GDGTs with cyclopentane rings (5/(1+2+3+5)) to the calcium concentration of individual samples. *Iso*GDGT-4 was excluded from this ratio due to the co-elution with the $[M+H]^+ + 2$ ion of crenarchaeol that also gives *m/z* 1294[S47].

Calcium concentrations in peats are a good indicator of nutrient content and alkalinity (pH) in these peats[S48]. Calcium concentrations are low, typically less than 500 mg/kg dry peat, in nutrient-poor ombrotrophic bogs. River-influenced nutrient-rich minerotrophic peats with pH > 5 are characterized by much higher calcium concentrations, up to 17,000 mg/kg dry peat[S48,49]. When we plot the 5/(1+2+3+5) ratio against calcium concentration for individual peat samples (Fig. S7), it is clear that *iso*GDGT-5 is only present in samples with a low calcium content (< 2000 mg/kg, mostly < 500 mg/kg dry peat) and hence low pH. The CBTpeat'-based pH calibration for peats has a relatively large error of ±0.8 pH units and caution should be taken with applying CBTpeat' to reconstruct absolute pH-values[S43]. Even so, the CBT_{peat}' based pH values for these samples support the inferences derived from Ca ratios. *iso*GDGT-5 is only present in samples with CBT_{peat}'-based pH < 5 and predominantly in samples with CBT'peat-based pH < 4, as seen in the global dataset (Fig. 2 of the main manuscript).

In addition, a 750 cm long peat core from the Aucayacu peatland is characterized by a shift in peat forming environment. Sediments spanning 9 to 5 ka (below 400 cm) formed under minerotrophic conditions with high calcium concentrations (high pH), transitioning to low calcium concentrations (low pH) in the upper 400 cm spanning the late Holocene (last 5 kyr)[S48,50]. This transition occurred as

the peat deposit grew higher, out of river influence and into ombrotropic conditions. *iso*GDGT-5 is only present in the ombrotrophic (low pH), upper 400 cm of the core and absent in the underlying minerotrophic (high pH) peat (Fig. S8). Together, the modern surface samples and downcore results indicate a clear pH dependence controlling the abundance of *iso*GDGT-5.

TEX_{86}[S38] and the ring index (RI)[S36], established indices that reflect the degree of cyclisation of *iso*GDGTs, did not correlate with pH (Fig. S9).

$$TEX_{86} = \frac{(isoGDGT\_2 + isoGDGT\_3 + cren.isomer.)}{(isoGDGT\_1 + isoGDGT\_2 + isoGDGT\_3 + cren.isomer.)}$$

$$\text{Ring index} = \frac{\left(isoGDGT\_1 + 2 \times isoGDGT\_2 + 3 \times isoGDGT\_3 + 4 \times (cren. + cren.isomer)\right)}{(isoGDGT\_0 + isoGDGT\_1 + isoGDGT\_2 + isoGDGT\_3 + cren. + cren.isomer)}$$

3.2 Temperature dependence

Although the relationship differs between settings, both in culture experiments of hyperthermophiles and incubation experiments of mesophiles[S36,40] as well as natural archives such as marine[S38] and lake sediments[S51] and hot springs[S34,41] the degree of cyclization of *iso*GDGTs, reflected in RI and/or TEX_{86}, is positively correlated with growth temperature. So far it is largely unknown whether the cyclization of *iso*GDGTs in terrestrial settings is correlated to growth temperature, although there is some recent evidence that suggests that *iso*GDGTs in mineral soil altitude transects from Tanzania and China differ according to temperature[S52,53].

Our results demonstrate that individual *iso*GDGTs with 0-3 cyclopentane rings have either no or weak ($0.1 < R^2 < 0.2$) correlations with MAAT (Fig. S10). Also RI (with or without crenarchaeol) and TEX_{86} have no clear correlation with MAAT (Fig. S11). The lack of correlation between the distribution of *iso*GDGTs and MAAT is likely because the *iso*GDGT pool is derived from a mixture of GDGT-producing archaeal communities that thrive in peats. In regular marine sediments, the majority of GDGTs are derived from (planktonic) marine Thaumarchaeota that modify their membrane lipids depending on temperature, reflected in the TEX_{86} proxy. However the dominance of *iso*GDGT-0 and low abundance of crenarchaeol in almost all peat samples, and resulting consistently low ring index, suggests a dominance of methanogenic Euryarchaeota. Consistent with this, if ring indices are calculated, excluding crenarchaeol, they remain poorly correlated to temperature and pH.

For *iso*GDGT-5 there is currently not enough data to construct a temperature calibration, especially due to the additional influence of pH on the relative abundance of *iso*GDGT-5 (see section 3.1). However, *iso*GDGT-5 is absent in ombrotrophic peats from the mid and high latitudes with MAAT < 12 °C. The highest relative abundance of *iso*GDGT-5 occurs in tropical peats accumulating under highest MAAT, indicating a temperature influence on the relative abundance of *iso*GDGT-5 (Fig. S10).

A combined pH/temperature control on the distribution of *iso*GDGT-5 is supported by four decades of research that reveal a pH and growth temperature dependence on *iso*GDGTs in cultures of acidohyperthermophilic Archaea[S36] and mesocosm experiments of marine Thaumarchaeota[S40], as well as the observed correlation between the degree of cyclization and temperature and/or pH in natural environments such as hot springs[S34] and the open ocean[S38]. Amongst cultured organisms, Euryarchaeota belonging to the order Thermoplasmatales as well as Crenarchaeota of the orders Thermoproteales and Sulfolobales are the only known source organisms of *iso*GDGT-5 to -8[S42]; therefore, it is possible that (uncultured mesophilic) relatives of these specific orders are responsible for the presence of *iso*GDGT-5 to -7 in our modern ombrotrophic tropical peats and early Paleogene lignites.

4. Environmental controls on the *br*GDGT distribution in modern peat

*br*GDGTs are membrane-spanning lipids produced by bacteria, likely acidobacteria[S54-56]. A decade of research has demonstrated that in mineral soils and lakes the degree of methylation of bacterial *br*GDGTs depends on temperature[S57-60]. We recently expanded this by developing a global peat-specific *br*GDGT temperature calibration that is based on the degree of methylation of *br*GDGTs, reflected in the MBT'_{5me} index[S57], in 470 samples from 96 different of modern peats: $MAAT_{peat}$[S43]. Importantly, the *br*GDGT data for this peat calibration dataset was generated using the latest HPLC-MS methods[S61] that separate the recently discovered 5- and 6-methyl *br*GDGTs[S62].

$$MBT'_{5me} = \frac{(Ia + Ib + Ic)}{(Ia + Ib + Ic + IIa + IIb + IIc + IIIa)}$$

$$MAAT_{peat}\ (°C) = 52.18 \times MBT'_{5me} - 23.05\ (n = 96, \quad R^2 = 0.76,$$

$$RMSE = 4.7\ °C)$$

In addition, the degree of cyclization of *br*GDGTs in mineral soils can be used to reconstruct pH[S57,58]. We recently demonstrated that also in peat the degree of cyclization of *br*GDGTs, expressed in the CBT_{peat} index, is correlated with pH[S43], although the correlation is weaker compared to that seen in mineral soils.

$$CBT_{peat} = \log\frac{(Ib + IIa' + IIb + IIb' + IIIa')}{(Ia + IIa + IIIa)}$$

$$pH = 2.49 \times CBT_{peat} + 8.07 \; (n = 51, \quad R^2 = 0.58, \quad RMSE = 0.8)$$

As lignites are formed from compaction of peat under low burial pressure and temperatures, we apply this peat-specific calibration to reconstruct terrestrial temperatures during the early Paleogene. Inherent to this approach is the assumption that the relationship between MBT'_{5me} and temperature was the same during the early Paleogene as at present.

GDGTs can be influenced by thermal maturation. Schouten et al.[S42,63] showed that *iso*- and *br*GDGTs are similarly influenced by thermal degradation as GDGTs disappear at hydrous pyrolysis temperatures > 260 °C. Consistent with these experiments, GDGTs appear to be absent in thermally mature coal[S64]. In addition, thermal maturation of GDGTs between ~220 and 260 °C was shown to influence their distribution, with a decrease in the degree of methylation and cyclization[S42,63]. Thus, thermal maturation can not explain the high temperatures we reconstruct for the early Paleogene using lignites as 1) lignites are formed a low burial temperatures (<100 °C) where GDGTs are not influenced, and 2) if thermal degradation would have influenced the *br*GDGTs in our lignites, this would have lowered MBT'_{5me} and hence resulted in low $MAAT_{peat}$.

5. GDGT distribution early Paleogene lignites

As explained in the previous section, we assume that the relationship observed in modern peat between MBT'_{5me} and temperature[S43] was the same during the early Paleogene. This assumption is supported by the observation that the broader GDGT distribution in our lignites, of which the majority formed between 45 and 60 degrees latitude during the early Paleogene, is very similar to modern-day distribution of GDGTs in tropical peats. The lignite and tropical modern-day peat are characterized by a high abundance of *iso*GDGTs with cyclopentane rings (including *iso*GDGT-5), H-*iso*GDGTs[S44] (characterized by a covalent bond between the two alkyl chains[S65]), and dominance of *br*GDGT-Ia over the other *br*GDGTs. On the other hand, the

GDGT distribution in our lignites looks different compared to a modern-day mid-latitude peat (Fig. S12). Modern-day mid-latitude peats lack significant amounts of *iso*GDGTs with cyclopentane rings, do not contain *iso*GDGT-5 or H-*iso*GDGTs, and penta- and hexamethylated *br*GDGT are abundant.

Sinninghe Damsté[S66] recently used a ternary plot of the *br*GDGT distribution in marine sediments and argued that samples that plot off the *br*GDGT distribution seen in the modern mineral soil database contain a contribution of *in situ br*GDGT production and do not exclusively contain mineral soil-derived terrestrial *br*GDGTs. Following this approach, if the GDGT distribution of our early Paleogene lignites was not produced in peats, the lignite data should plot outside of distribution of *br*GDGTs in the modern peat database. However, when we compare the *br*GDGT distribution in our early Paleogene lignites to that of modern peats[S43] using ternary plots (Fig. S13), it is clear that the *br*GDGT distribution of early Paleogene lignites looks very similar to that in modern peatlands. We then extended this approach by comparing the *iso*GDGT distribution in our early Paleogene lignites with that seen in modern peats and marine core-top sediments (Fig. S14). The *iso*GDGT distribution in our early Paleogene lignites looks very similar to that seen in modern-day peats with a very low proportion of crenarchaeol and looks very different from the *iso*GDGT distribution of for example marine sediments[S67]. These results highlight that not only MBT'$_{5me}$ (and hence MAAT$_{peat}$) and the abundance of *iso*GDGT-5 in our early Paleogene lignites are similar to modern (tropical) peats, but that the broader GDGT distribution of our early Paleogene lignites is comparable to a modern-day (tropical) peat.

The only difference is the abundance of *iso*GDGT-5 encountered in the Indian lignites, which is higher than found in any modern peat, even in modern tropical peats (MAAT ~ 26.5 °C) with pH ~ 3. As pH of 3 is the most acidic peat environment known, the higher abundance of *iso*GDGT-5 found in the Indian lignites is at least party related to temperatures higher than MAAT > 26.5 °C, inline with our MAAT$_{peat}$ temperature estimates. In addition, it is unlikely that the high abundance of *iso*GDGT-5 in the Indian lignites (compared to the mid-latitude lignites) is the result of a much lower pH. For example there is independent evidence that at least some of the mid-latitude lignites were formed in ombrotrophic (low pH) *Sphagnum* peats[S4] and CBT$_{peat}$' is similar for all lignites.

6. Calculation of paleolatitudes

To be consistent the Ypresian paleolatitudes for all published terrestrial (and marine) sites as well as the lignites were (re)calculated using the models explained in[S68]. These paleolatitudes might differ sligthtly form those reported in the original publications. The uncertainty in the paleolatitude calculations for each site is not known, but can be up to several degrees paleolatitude.

7. Compilation of published early Paleogene terrestrial temperatures

We compiled terrestrial temperature data based on a range of proxy methods as plotted in figure 1. The majority of data is obtained using leaf physiognomy from the early Paleogene (late Paleocene and early Eocene) and derived mainly from the Huber and Caballero[S69] and Yang et al.[S70] compilations (see data file). There are different leaf physiognomy methods and we grouped them into three groups 1) data obtained using the Kowalski and Ditcher (K&D) leaf margin analysis calibration[S71] , 2) data obtained using Climate Leaf Analysis Multivariate Program (CLAMP), and 3) other leaf physiognomy data (e.g. using alternative leaf margin analysis calibrations[S72]). Estimates based on nearest living relatives data from plants (e.g. coexistence approach, bioclimatic analysis, etc) were omitted from figure 1 and 3 because of their reliance on correct identification of the nearest living relative. For comparison, figures S15 and S16 include this nearest living relative tempeature data. In addition, we omitted a number of data points from the various compilations either because the data was confirmed to be middle Eocene in age (Axel Heidelberg, Geiseltal, Puryear-Buchanan, Kisinger Lakes, Chermurnaut Bay, Fossil Hill Flora - King George Island, and James Ross Basin), represented the PETM (Dragon Glacier - King George Island, Hubble Bubble – Bighorn Basin), the age of the data was poorly constrained (Mahenge and Raichikha), or because the altitude correction applied was uncertain (China Gulch, Camanche Bridge, Pentz, Cherokee Site 1, Fiona Hill, Council Hill, Iowa Hill, You Bet 2, Chalk Bluffs – E., Scotts Flat, Gold Bug, Hidden Gold Camp, Woolsey Flat, Mountain Boy, and Pine Grove 1). From Yang et al.[S70] we used the gridded data adjusted.

Where available we show MAAT obtained using different calibrations to show the full uncertainty regarding leaf physiognomy based MAATs. For Climate Leaf Analysis Multivariate Program (CLAMP) data[S70] we use an uncertainty of ± 2 °C (http://clamp.ibcas.ac.cn/CLAMP_Uncertainties.html). We want to highlight that use of the Kowalski and Ditcher (K&D) calibration used in Huber and Caballero[S69] often

does lead to higher MAAT estimates compared to other calibrations (e.g. CLAMP), but it is based on a very limited dataset.

All the previously published MBT/CBT-based mineral soil-derived MAAT[S31,73-77], based on the distribution of *br*GDGTs in (proximal) marine sediments, were revised using the updated MBT'/CBT calibration[S78]. The errors shown in figure 1 for the MBT'/CBT based data were obtained by adding the 5 °C calibration error of the MBT'/CBT calibration[S78] to the one standard deviation of the MBT'/CBT data for each site. For $MAAT_{peat}$ the error bars were calculated the same way, but using a calibration error of 4.7 °C[S43]. Only data spanning the late Paleocene and early Eocene (57-48 Myr) was used (see data file). Where the PETM was recognized; data from the PETM was excluded.

We also included temperature data from early Paleogene paleosols from Argentina[S79] and the USA[S80] as well as early Paleogene $\delta^{18}O$-based terrestrial temperatures from mammalian tooth enamel and fish (gar) scales, all from the Northern Hemisphere[S81,82].

8. Compilation of published early Paleogene sea surface temperatures

To compare our early Paleogene terrestrial temperature data with sea surface temperature (SST) data, we compiled all available published data based on the organic geochemical TEX_{86} palaeothermometer as well as calcite-based SSTs using Mg/Ca and $\delta^{18}O$ of pristine planktonic foraminifera and clumped isotopes (see data file). TEX_{86}-based SSTs were calculated using the BAYSPAR deep time analog approach[S67,83]. Error bars on TEX_{86}-based SST in figure 1 represent the 1σ confidence interval. For the calcite-based proxies the errors were calculated by combining the calibration error and the one standard deviation of the data for each site under different assumptions of early Paleogene seawater composition; $-0.64 < \delta^{18}O_{sw}$ (VSMOW) < -0.21[S84] and $1.5 < (Mg/Ca)_{sw} < 5$[S85]. Only data spanning the late Paleocene and early Eocene (57-48 Myr) was used (see data file). Where the PETM was recognized SST data from the PETM was excluded.

9. Data model comparison

The model-data comparison shown in Figure 3 is carried out using identical methods to those outlined in Lunt et al.[S84]. In brief, the early Paleogene zonal mean near-surface (~2m) continental air temperature is calculated for each of 7 models using

different pCO_2 concentrations; $2xCO_2$ ECHAM5[S86], $2xCO_2$ FAMOUS[S87], $4xCO_2$ GISS[S88], $5xCO_2$ CCSM3_K[S89], $6xCO_2$ HadCM3L[S90], $16xCO_2$ CCSM3_W[S91] and $16xCO_2$ CCSM3_H[S69]. The prescribed Eocene paleogeography also varies across the simulations as shown in the relevant references cited above.

An equivalent temperature (but global rather than continental) from an equivalent preindustrial simulation from each model is also calculated, and the difference, early Paleogene minus pre-industrial, is shown as coloured lines in Figure 3. In the nomenclature of Lunt et al.[S84], this is $\left[\overline{LAT_{ep}} - \overline{GAT_p}\right]$. On top of these modelled zonal mean anomalies, our compilation of proxy early Paleogene terrestrial temperatures is plotted, including our new $MAAT_{peat}$ estimates, and including published estimates of uncertainties. These proxy temperatures are plotted as anomalies relative to the zonal mean of observed modern global (not exclusively terrestrial) near-surface air temperatures, (NCEP[S92]), for the period 1981–2010. As such, the proxy data represent temperature anomalies at a single site, whereas the modelled results are zonal means.

Supplementary references

S1 Robson, B. E. *et al.* Early Paleogene wildfires in peat-forming environments at Schöningen, Germany, *Palaeogeogr. Palaeoclimatol. Palaeoecol.* **437**, 53-62, (2015).

S2 Inglis, G. N. *et al.* Mid-latitude continental temperatures through the early Eocene in western Europe, *Earth Plant. Sc. Lett.* **460**, 86-96, (2017).

S3 Riegel, W., Wilde, V. & Lenz, O. K. The early Eocene of Schöningen (N-Germany) - an interim report, *Aust. J. Earth Sci.* **105**, 88-109, (2012).

S4 Inglis, G. N. *et al.* Ecological and biogeochemical change in an early Paleogene peat-forming environment: Linking biomarkers and palynology, *Palaeogeogr. Palaeoclimatol. Palaeoecol.* **438**, 245-255, (2015).

S5 Ahrendt, H., Köthe, A., Lietzow, A., Marhein, D. & Ritzkowski, S. Lithostratigraphy, biostratigraphy and radiometric dating of the Early Eocene at Helmstedt (Lower Saxony), *Z. Dtsch. Geol. Ges.* **146**, 450-457, (1995).

S6 Crouch, E. M. *et al.* The *Apectodinium* acme and terrestrial discharge during the Paleocene–Eocene thermal maximum: new palynological, geochemical and calcareous nannoplankton observations at Tawanui, New Zealand, *Palaeogeogr. Palaeoclimatol. Palaeoecol.* **194**, 387-403, (2003).

S7 Sluijs, A. *et al.* Environmental precursors to rapid light carbon injection at the Palaeocene/Eocene boundary, *Nature* **450**, 1218-1221, (2007).

S8 Pancost, R. D. *et al.* Increased terrestrial methane cycling at the Palaeocene-Eocene thermal maximum, *Nature* **449**, 332-335, (2007).

S9 Collinson, M. E., Hooker, J. J. & Gröcke, D. R. in *Causes and Consequences of Globally Warm Climates in the Early Paleogene* Vol. 369 (eds Scott L. Wing, P.D. Gingerich, B. Schmitz, & B. Thomas) 333-349 (Geological Society of America, 2003).

S10 Collinson, M. E. *et al.* Palynological evidence of vegetation dynamics in response to palaeoenvironmental change across the onset of the Paleocene – Eocene Thermal Maximum at Cobham, Southern England, *Grana* **48**, 38-66, (2009).

S11 Biswas, S. K. Tertiary stratigraphy of Kutch, *J. Palaeontol. Soc. Ind.* **37**, 1-29, (1992).

S12 Sahni, N., Rose, K. D., Singh, L. & Smith, T. Temporal constraints and depositional paleoenvironments of the Vastan lignite sequences, Gujarat: Analogy for Cambay shale Hydrocarbon source rock, *Indian J. Petrol. Geol.* **15**, 1-20, (2006).

S13 McCann, T. Chenier plain sedimentation in the Palaeogene-age lignite-rich successions of the Surat area, Gujarat, western India, *Z. Dtsch. Geol. Ges.* **161**, 335-351, (2010).

S14 Singh, P. K. *et al.* Petrological and Geochemical Investigations of Rajpardi Lignite Deposit, Gujarat, India, *Energ. Explor. Exploit.* **30**, 131-151, (2012).

S15 Singh, A. K., Singh, M. P. & Singh, P. K. Petrological investigations of Oligocene coals from foreland basin of northeast India, *Energ. Explor. Exploit.* **31**, 909-936, (2013).

S16 Singh, P. K., Singh, M. P. & Singh, A. K. Petro-chemical characterization and evolution of Vastan Lignite, Gujarat, India, *Int. J. Coal Geol.* **82**, 1-16, (2010).

S17 Singh, P. K., Rajak, P. K., Singh, M. P., Singh, V. K. & Naik, A. S. Geochemistry of Kasnau-Matasukh lignites, Nagaur basin, Rajasthan (India), *Inter. J. Coal Sc. Tech.* **3**, 104-122, (2016).

S18 Singh, P. K. *et al.* Peat swamps at Giral lignite field of Barmer basin, Rajasthan, Western India: Understanding the Evolution through Petrological Modelling, *Inter. J. Coal Sc. Tech.* **3**, 148-164, (2016).

S19 Dutta, S. *et al.* Petrology, palynology and organic geochemistry of Eocene lignite of Matanomadh, Kutch Basin, western India: Implications to depositional environment and hydrocarbon source potential, *Int. J. Coal Geol.* **85**, 91-102, (2011).

S20 Mathews, R. P., Tripathi, S. M., Banerjee, S. & Dutta, S. Palynology, palaeoecology and palaeodepositional environment of Eocene lignites and associated sediments from Matanomadh mine, Kutch Basin, western India, *J. Geol. Soc. India* **82**, 236-248, (2013).

S21 Samant, B. Palynostratigraphy and age of the Bhavnagar lignite, Gujarat, India, *Palaeobotanist* **49**, 101-108, (2000).

S22 Samant, B. Fungal remains from the Bhavnagar lignite, Gujarat, India, *Geophytology* **28**, 11-18, (2000).

S23 Thakur, O. P., Singh, A. & Singh, B. D. Petrographic characterization of Khadsaliya lignites, Bhavnagar district, Gujarat, *J. Geol. Soc. Inia* **76**, 40-46, (2010).

S24 La Touche, T. D. Report on the Occurrence of coal at Palana village in Bikaner State, *Record of the Geological Society of India* **30**, (1897).

S25 Rao, S. R. N. & Vimal, K. P. Tertiary pollen from lignite from Palana (Eocene) Bikaner, *Proc. Nat. Instit. Sci. India* **18**, 595-601, (1952).
S26 Tripathi, R. P., Si Sodia, M. S., Srivastava, K. L. & Sharma, B. D. in *Geological evolution of northwestern India* (ed B.S. Paliwal) 118–128 (Scientific Publishers, 1999).
S27 Singh, S. N. Planktonic foraminifera in the Eocene stratigraphy of Rajasthan, India, *roceedings of the 2nd International Conference on Planktonic Microfossils, Rome* **2**, 1169–1181, (1971).
S28 Tripathi, S. K. M., Mathur, S. C., Nama, S. L. & Srivastava, D. in *Palaeobotany to modern botany* (ed P.C. Trivedi) 49–56 (Pointer Publishers, 2006).
S29 Kumar, K., Rana, R. S. & Paliwal, B. S. Osteoglossid and lepisosteid fish remains from the Paleocene Palana formation, Rajasthan, India, *Palaeontology* **48**, 1187–1209, (2005).
S30 Field, B. D., Browne, G. H. & Davy, B. W. Cretaceous and Cenozoic sedimentary basins and geological evolution of the Canterbury region, South Island, New Zealand, (New Zealand Geological Survey, 1989).
S31 Pancost, R. D. *et al.* Early Paleogene evolution of terrestrial climate in the SW Pacific, Southern New Zealand, *Geochem. Geophys. Geosyst.* **14**, 5413-5429, (2013).
S32 Raine, J. I. *et al.* New Zealand Geological Timescale NZGT 2015/1, *New Zeal. J. Geol. Geop.* **58**, 398-403, (2015).
S33 Pearson, A. & Rusch, D. B. Distribution of microbial terpenoid lipid cyclases in the global ocean metagenome, *ISME J.* **3**, 352-363, (2008).
S34 Kaur, G., Mountain, B., Stott, M., Hopmans, E. & Pancost, R. Temperature and pH control on lipid composition of silica sinters from diverse hot springs in the Taupo Volcanic Zone, New Zealand, *Extremophiles* **19**, 327-344, (2015).
S35 Shimada, H., Nemoto, N., Shida, Y., Oshima, T. & Yamagishi, A. Effects of pH and Temperature on the Composition of Polar Lipids in Thermoplasma acidophilum HO-62, *J. Bacteriol.* **190**, 5404-5411, (2008).
S36 De Rosa, M., Esposito, E., Gambacorta, A., Nicolaus, B. & Bu'Lock, J. D. Effects of temperature on ether lipid composition of *Caldariella acidophila*, *Phytochemistry* **19**, 827-831, (1980).
S37 De Rosa, M. & Gambacorta, A. The lipids of archaebacteria, *Prog. Lipid Res.* **27**, 153-175, (1988).
S38 Schouten, S., Hopmans, E. C., Schefuss, E. & Sinninghe Damsté, J. S. Distributional variations in marine crenarchaeotal membrane lipids: a new tool for reconstructing ancient sea water temperatures?, *Earth Plant. Sc. Lett.* **204**, 265-274, (2002).
S39 Elling, F. J., Könneke, M., Mußmann, M., Greve, A. & Hinrichs, K.-U. Influence of temperature, pH, and salinity on membrane lipid composition and TEX_{86} of marine planktonic thaumarchaeal isolates, *Geochim. Cosmochim. Acta* **171**, 238-255, (2015).
S40 Schouten, S., Forster, A., Panoto, F. E. & Sinninghe Damsté, J. S. Towards calibration of the TEX_{86} palaeothermometer for tropical sea surface temperatures in ancient greenhouse worlds, *Org. Geochem.* **38**, 1537-1546, (2007).

S41 Pearson, A. *et al.* Factors Controlling the Distribution of Archaeal Tetraethers in Terrestrial Hot Springs, *Appl. Environ. Microbiol.* **74**, 3523-3532, (2008).
S42 Schouten, S., Hopmans, E. C. & Sinninghe Damsté, J. S. The organic geochemistry of glycerol dialkyl glycerol tetraether lipids: A review, *Org. Geochem.* **54**, 19-61, (2013).
S43 Naafs, B. D. A. *et al.* Introducing global peat-specific temperature and pH calibrations based on brGDGT bacterial lipids, *Geochim. Cosmochim. Acta* **208**, 285-301, (2017).
S44 Naafs, B. D. A., McCormick, D., Inglis, G. N. & Pancost, R. D. Archaeal and bacterial H-GDGTs are abundant in peat and their relative abundance is positively correlated with temperature, *Geochim. Cosmochim. Acta* **227**, 156-170, (2018).
S45 Wu, W. *et al.* Impacts of temperature and pH on the distribution of archaeal lipids in Yunnan hot springs, China, *Front. Microbiol.* **4**, 312, (2013).
S46 Xie, W., Zhang, C. & Ma, C. Temporal variation in community structure and lipid composition of Thaumarchaeota from subtropical soil: Insight into proposing a new soil pH proxy, *Org. Geochem.* **83–84**, 54-64, (2015).
S47 Weijers, J. W. H., Schouten, S., van der Linden, M., van Geel, B. & Sinninghe Damsté, J. S. Water table related variations in the abundance of intact archaeal membrane lipids in a Swedish peat bog, *FEMS Microbiol. Lett.* **239**, 51-56, (2004).
S48 Lähteenoja, O. & Page, S. High diversity of tropical peatland ecosystem types in the Pastaza-Marañón basin, Peruvian Amazonia, *J. Geophys. Res. Biogeosci.* **116**, (2011).
S49 Lähteenoja, O., Ruokolainen, K., Schulman, L. & Alvarez, J. Amazonian floodplains harbour minerotrophic and ombrotrophic peatlands, *Catena* **79**, 140-145, (2009).
S50 Lähteenoja, O. *et al.* The large Amazonian peatland carbon sink in the subsiding Pastaza-Marañón foreland basin, Peru, *Global Change Biol.* **18**, 164-178, (2012).
S51 Powers, L. *et al.* Applicability and calibration of the TEX_{86} paleothermometer in lakes, *Org. Geochem.* **41**, 404-413, (2010).
S52 Coffinet, S., Huguet, A., Williamson, D., Fosse, C. & Derenne, S. Potential of GDGTs as a temperature proxy along an altitudinal transect at Mount Rungwe (Tanzania), *Org. Geochem.* **68**, 82-89, (2014).
S53 Yang, H., Pancost, R. D., Jia, C. & Xie, S. The Response of Archaeal Tetraether Membrane Lipids in Surface Soils to Temperature: A Potential Paleothermometer in Paleosols, *Geomicrobiol. J.* **33**, 98-109, (2016).
S54 Weijers, J. W. H. *et al.* Membrane lipids of mesophilic anaerobic bacteria thriving in peats have typical archaeal traits, *Environ. Microbiol.* **8**, 648-657, (2006).
S55 Sinninghe Damsté, J. S. *et al.* 13,16-Dimethyl Octacosanedioic Acid (*iso*-Diabolic Acid), a Common Membrane-Spanning Lipid of *Acidobacteria* Subdivisions 1 and 3, *Appl. Environ. Microb.* **77**, 4147-4154, (2011).
S56 Sinninghe Damsté, J. S. *et al.* Ether- and Ester-Bound iso-Diabolic Acid and Other Lipids in Members of Acidobacteria Subdivision 4, *Appl. Environ. Microb.* **80**, 5207-5218, (2014).

S57 De Jonge, C. *et al.* Occurrence and abundance of 6-methyl branched glycerol dialkyl glycerol tetraethers in soils: implications for palaeoclimate reconstruction, *Geochim. Cosmochim. Acta* **141**, 97-112, (2014).

S58 Weijers, J. W. H., Schouten, S., van den Donker, J. C., Hopmans, E. C. & Sinninghe Damsté, J. S. Environmental controls on bacterial tetraether membrane lipid distribution in soils, *Geochim. Cosmochim. Acta* **71**, 703-713, (2007).

S59 Naafs, B. D. A., Gallego-Sala, A. V., Inglis, G. N. & Pancost, R. D. Refining the global branched glycerol dialkyl glycerol tetraether (brGDGT) soil temperature calibration, *Org. Geochem.* **106**, 48-56, (2017).

S60 Loomis, S. E., Russell, J. M., Ladd, B., Street-Perrott, F. A. & Sinninghe Damsté, J. S. Calibration and application of the branched GDGT temperature proxy on East African lake sediments, *Earth Planet. Sc. Lett.* **357–358**, 277-288, (2012).

S61 Hopmans, E. C., Schouten, S. & Sinninghe Damsté, J. S. The effect of improved chromatography on GDGT-based palaeoproxies, *Org. Geochem.* **93**, 1-6, (2016).

S62 De Jonge, C. *et al.* Identification of novel penta- and hexamethylated branched glycerol dialkyl glycerol tetraethers in peat using HPLC–MS^2, GC–MS and GC–SMB-MS, *Org. Geochem.* **54**, 78-82, (2013).

S63 Schouten, S., Hopmans, E. C. & Sinninghe Damsté, J. S. The effect of maturity and depositional redox conditions on archaeal tetraether lipid palaeothermometry, *Org. Geochem.* **35**, 567-571, (2004).

S64 Weijers, J. W. H., Steinmann, P., Hopmans, E. C., Schouten, S. & Sinninghe Damsté, J. S. Bacterial tetraether membrane lipids in peat and coal: Testing the MBT-CBT temperature proxy for climate reconstruction, *Org. Geochem.* **42**, 477-486, (2011).

S65 Morii, H. *et al.* A novel ether core lipid with H-shaped C_{80}-isoprenoid hydrocarbon chain from the hyperthermophilic methanogen *Methanothermus fervidus*, *BBA-Lipid Lipid Met.* **1390**, 339-345, (1998).

S66 Sinninghe Damsté, J. S. Spatial heterogeneity of sources of branched tetraethers in shelf systems: The geochemistry of tetraethers in the Berau River delta (Kalimantan, Indonesia), *Geochim. Cosmochim. Acta* **186**, 13-31, (2016).

S67 Tierney, J. E. & Tingley, M. P. A TEX_{86} surface sediment database and extended Bayesian calibration, *Sci. Data* **2**, 150029, (2015).

S68 Lunt, D. J. *et al.* Palaeogeographic controls on climate and proxy interpretation, *Clim. Past* **12**, 1181-1198, (2016).

S69 Huber, M. & Caballero, R. The early Eocene equable climate problem revisited, *Clim. Past* **7**, 603-633, (2011).

S70 Yang, J., Spicer, R. A., Spicer, T. E. V. & Li, C.-S. 'CLAMP Online': a new web-based palaeoclimate tool and its application to the terrestrial Paleogene and Neogene of North America, *Palaeobiodivers. palaeoenviron.* **91**, 163-183, (2011).

S71 Kowalski, E. A. & Dilcher, D. L. Warmer paleotemperatures for terrestrial ecosystems, *Proc. Natl. Acad. Sci.* **100**, 167-170, (2003).

S72 Peppe, D. J. *et al.* Sensitivity of leaf size and shape to climate: global patterns and paleoclimatic applications, *New Phytol.* **190**, 724-739, (2011).
S73 Weijers, J. W. H., Schouten, S., Sluijs, A., Brinkhuis, H. & Sinninghe Damsté, J. S. Warm arctic continents during the Palaeocene–Eocene thermal maximum, *Earth Planet. Sc. Lett.* **261**, 230-238, (2007).
S74 Sluijs, A. *et al.* Warming, euxinia and sea level rise during the Paleocene–Eocene Thermal Maximum on the Gulf Coastal Plain: implications for ocean oxygenation and nutrient cycling, *Clim. Past* **10**, 1421-1439, (2014).
S75 Keating-Bitonti, C. R., Ivany, L. C., Affek, H. P., Douglas, P. & Samson, S. D. Warm, not super-hot, temperatures in the early Eocene subtropics, *Geology* **39**, 771-774, (2011).
S76 Bijl, P. K. *et al.* Eocene cooling linked to early flow across the Tasmanian Gateway, *P. Natl. Acad. Sci. USA* **110**, 9645-9650, (2013).
S77 Schoon, P. L., Heilmann-Clausen, C., Schultz, B. P., Sinninghe Damsté, J. S. & Schouten, S. Warming and environmental changes in the eastern North Sea Basin during the Palaeocene–Eocene Thermal Maximum as revealed by biomarker lipids, *Org. Geochem.* **78**, 79-88, (2015).
S78 Peterse, F. *et al.* Revised calibration of the MBT–CBT paleotemperature proxy based on branched tetraether membrane lipids in surface soils, *Geochim. Cosmochim. Acta* **96**, 215-229, (2012).
S79 Hyland, E. G., Sheldon, N. D. & Cotton, J. M. Constraining the early Eocene climatic optimum: A terrestrial interhemispheric comparison, *Geol. Soc. Am. Bull.* **129**, 244-252, (2017).
S80 Hyland, E., Sheldon, N. D. & Fan, M. Terrestrial paleoenvironmental reconstructions indicate transient peak warming during the early Eocene climatic optimum, *Geol. Soc. Am. Bull.* **125**, 1338-1348, (2013).
S81 Hyland, E. G. & Sheldon, N. D. Coupled CO_2-climate response during the Early Eocene Climatic Optimum, **369**, 125-135, (2013).
S82 Fricke, H. C. & Wing, S. L. Oxygen isotope and paleobotanical estimates of temperature and $\delta^{18}O$–latitude gradients over North America during the early Eocene, *Am. J. Sci.* **304**, 612-635, (2004).
S83 Tierney, J. E. & Tingley, M. P. A Bayesian, spatially-varying calibration model for the TEX_{86} proxy, *Geochim. Cosmochim. Acta* **127**, 83-106, (2014).
S84 Lunt, D. J. *et al.* A model–data comparison for a multi-model ensemble of early Eocene atmosphere–ocean simulations: EoMIP, *Clim. Past* **8**, 1717-1736, (2012).
S85 Higgins, J. A. & Schrag, D. P. The Mg isotopic composition of Cenozoic seawater – evidence for a link between Mg-clays, seawater Mg/Ca, and climate, *Earth Planet. Sc. Lett.* **416**, 73-81, (2015).
S86 Heinemann, M., Jungclaus, J. H. & Marotzke, J. Warm Paleocene/Eocene climate as simulated in ECHAM5/MPI-OM, *Clim. Past* **5**, 785-802, (2009).
S87 Sagoo, N., Valdes, P., Flecker, R. & Gregoire, L. J. The Early Eocene equable climate problem: can perturbations of climate model parameters identify possible solutions?, *Philos. T. Roy. Soc. A* **371**, 0123, (2013).
S88 Roberts, C. D., LeGrande, A. N. & Tripati, A. K. Climate sensitivity to Arctic seaway restriction during the early Paleogene, *Earth Plant. Sc. Lett.* **286**, 576-585, (2009).

S89 Kiehl, J. T. & Shields, C. A. Sensitivity of the Palaeocene–Eocene Thermal Maximum climate to cloud properties, *Philos. T. Roy. Soc. A* **371**, 0093, (2013).
S90 Lunt, D. J. *et al.* CO_2-driven ocean circulation changes as an amplifier of Paleocene-Eocene thermal maximum hydrate destabilization, *Geology* **38**, 875-878, (2010).
S91 Winguth, A., Shellito, C., Shields, C. & Winguth, C. Climate Response at the Paleocene–Eocene Thermal Maximum to Greenhouse Gas Forcing—A Model Study with CCSM3, *J. Climate* **23**, 2562-2584, (2009).
S92 Kalnay, E. *et al.* The NCEP/NCAR 40-Year Reanalysis Project, *Bull. Am. Meteorol. Soc.* **77**, 437-471, (1996).
S93 Schlitzer, R. Ocean Data View, https://odv.awi.de, (2018).

Supplementary figure captions

Figure S1; Present-day location of the lignites used in this study. Map generated using ODV[S93].

Figure S2; HPLC-APCI-MS base peak chromatogram (top) and mass chromatograms of a tropical peat sample from Peru (the Aucayacu peatland, 330 cm depth). Numbers indicate number of cyclopentane moieties in the *iso*GDGTs, while roman numbers highlight the different *br*GDGTs. Cren = crenarchaeol and reg.iso= crenarchaeol regioisomer. In H-*iso*GDGTs the two biphytane chains are covalently bound by a carbon-carbon bond[S65].

Figure S3; HPLC-APCI-MS base peak chromatogram (top) and mass chromatograms of an early Paleogene lignite sample from Cobham (CL70, 11.95 cm). Numbers indicate number of cyclopentane moieties in the *iso*GDGTs, while roman numbers highlight the different *br*GDGTs. Cren = crenarchaeol and reg.iso= crenarchaeol regioisomer. In H-GDGTs the two biphytane chains are covalently bound by a carbon-carbon bond.

Figure S4; HPLC-APCI-MS base peak chromatograms of A) a tropical peat sample from Peru (the Aucayacu peatland, 330 cm depth), B) sample from the Champagne pool hot spring, and C) acid-hydrolized extract of the extremophile *Thermoplasma acidophilum*.

686 Figure S5; HPLC-APCI-MS base peak chromatograms of A) a tropical peat sample
687 from Peru (the Aucayacu peatland, 330 cm depth) and B) co-injection of the tropical
688 peat sample with the acid-hydrolized extract of the extremophile *Thermoplasma*
689 *acidophilum* that contains *iso*GDGT-5 but not crenarchaeol.
690
691 Figure S6; Fractional abundance of the individual *iso*GDGTs versus peat pH.
692 Horizontal bars reflect range of peat pH[S43], while vertical bars represent 1σ from the
693 average fractional abundance and are based on the analysis of multiple samples from
694 the same peatland. Fractional abundances < 0.001 are not shown.
695
696 Figure S7; Relative abundance of *iso*GDGT-5 (%) versus A) calcium content (a
697 measure of pH) for individual samples in a range of tropical peatlands from Peru that
698 all experience the same climate. (Ca content from[S48,49]) and B) CBT_{peat}-based pH.
699 Note that Ca data is not available for every sample.
700
701 Figure S8; Downcore relative abundance of *iso*GDGT-5 (%, orange) and calcium
702 content (mg/kg, blue) in the 750 cm long peat core from the Aucayacu peatland in
703 Peru that spans the last 9 kyr. Pie charts reflect the relative distribution of *iso*GDGTs
704 in the top and bottom of the peat. (Radiocarbon ages from[S50])
705
706 Figure S9; A) Ring index and B) TEX_{86} versus peat pH. Horizontal bars reflect range
707 of peat pH[S43], while vertical error bars represent 1σ from the average and are based on
708 the analysis of multiple samples from the same peatland.
709
710 Figure S10; Fractional abundance of the individual *iso*GDGTs versus overlying mean
711 annual air temperature. Vertical error bars represent 1σ from the average fractional
712 abundance and are based on the analysis of multiple samples from the same peatland.
713 Samples with a fractional abundance < 0.001 are not shown.
714
715 Figure S11; A) Ring index and B) TEX_{86} versus mean annual air temperature.
716 Vertical error bars represent 1σ from the average and are based on the analysis of
717 multiple samples from the same peatland.
718

719 Figure S12; HPLC-APCI-MS base peak chromatograms highlight the *iso*- and
720 *br*GDGT distribution in A) early Paleogene lignite from UK (Cobham CL70, 11.95
721 cm), B) modern mid-latitude peat samples from Germany (Bissendorfer Moor, 18 cm
722 depth), and C) modern tropical peat sample from Peru (the Aucayacu peatland, 330
723 cm depth). Modern MAAT Bissendorfer Moor and Aucayacu are 8.9 C and 26 °C,
724 while pH for these peats is 4 and 3.7, respectively.
725
726 Figure S13; Ternary plot of the *br*GDGT-distribution in the modern peat database[S43]
727 and all early Paleogene lignites used in this study. Plot shows the relative abundance
728 of the tetra- (*br*GDGT-Ia, -Ib, and Ic), penta- (*br*GDGT-IIa, -IIa', -IIb, -IIb', -IIc, and
729 -IIc'), and hexamethylated *br*GDGTs (*br*GDGT-IIIa, -IIIa', -IIIb, -IIIb', -IIIc, and -
730 IIIc').
731
732 Figure S14; Ternary plot of the *iso*GDGT-distribution in the modern peat database,
733 marine core-top sediments[S67], and all early Paleogene lignites used in this study. Plot
734 shows the relative abundance of the *iso*GDGT with no rings (*iso*GDGT-0), *iso*GDGTs
735 with 1 to 3 cyclopentane rings (*iso*GDGT-1, -2, and -3), and *iso*GDGT with a
736 cyclohexane ring (crenarchaeol).
737
738 Figure S15; Same as figure 1 of the main manuscript, but including estimates based
739 on nearest living relatives data (e.g. coexistence approach, bioclimatic analysis, etc.).
740 Leaf physiognomy methods: K&D - Kowalski and Ditcher leaf margin analysis
741 calibration[S71]; CLAMP - Climate Leaf Analysis Multivariate Program[S70]; other leaf
742 physiognomic - for example using alternative leaf margin analysis calibrations[S72] .
743 MAAT – mean annual air temperature.
744
745 Figure S16; Same as figure 3 of the main manuscript, but including estimates based
746 on nearest living relatives data (e.g. coexistence approach, bioclimatic analysis, etc.).
747 For abbreviations see Figure S15.
748
749 Figure S17; Global temperature anomaly between the early Paleogene and
750 present for all available terrestrial temperature data at the paleolatitude of each
751 location together with the zonal mean anomaly simulated by a range of climate

752 models; 2xCO_2 ECHAM5[S86], 2xCO_2 FAMOUS[S87], 4xCO_2 GISS[S88], 5xCO_2 CCSM3_K[S89],

753 6xCO_2 HadCM3L[S90], 16xCO_2 CCSM3_W[S91] and 16xCO_2 CCSM3_H[S69].

754

Figure S1

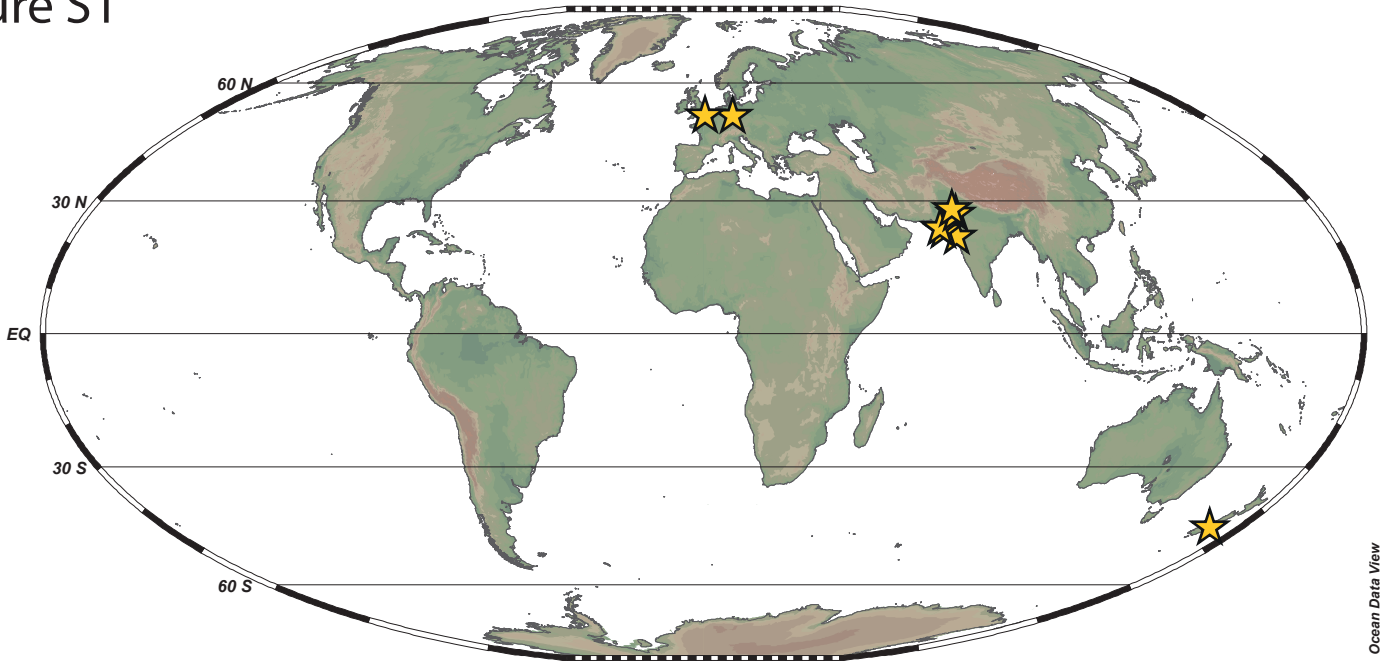

Figure S2

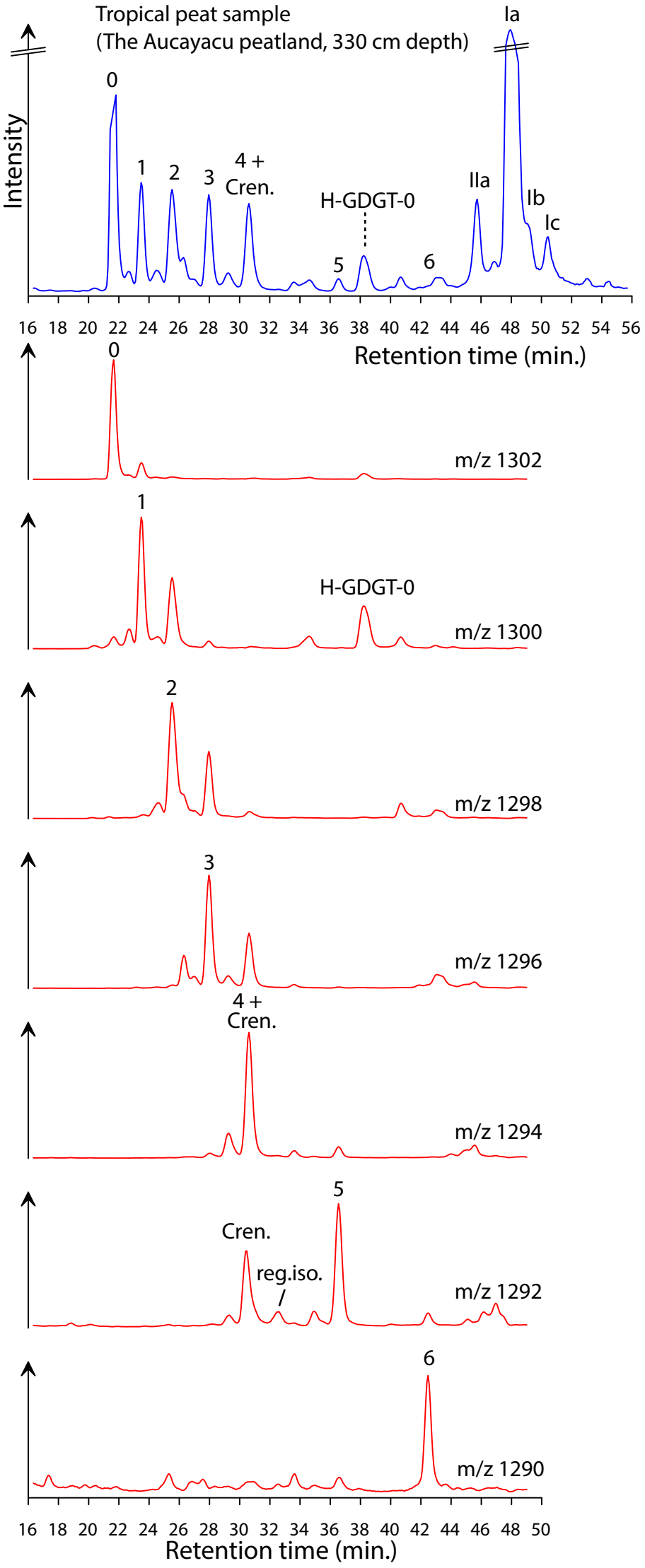
Tropical peat sample
(The Aucayacu peatland, 330 cm depth)
Intensity
0
1
2
3
4 +
Cren.
H-GDGT-0
5
6
IIa
Ia
Ib
Ic
16 18 20 22 24 26 28 30 32 34 36 38 40 42 44 46 48 50 52 54 56
Retention time (min.)
0
m/z 1302
1
H-GDGT-0
m/z 1300
2
m/z 1298
3
m/z 1296
4 +
Cren.
m/z 1294
5
Cren.
reg.iso.
m/z 1292
6
m/z 1290
16 18 20 22 24 26 28 30 32 34 36 38 40 42 44 46 48 50
Retention time (min.)

Figure S3

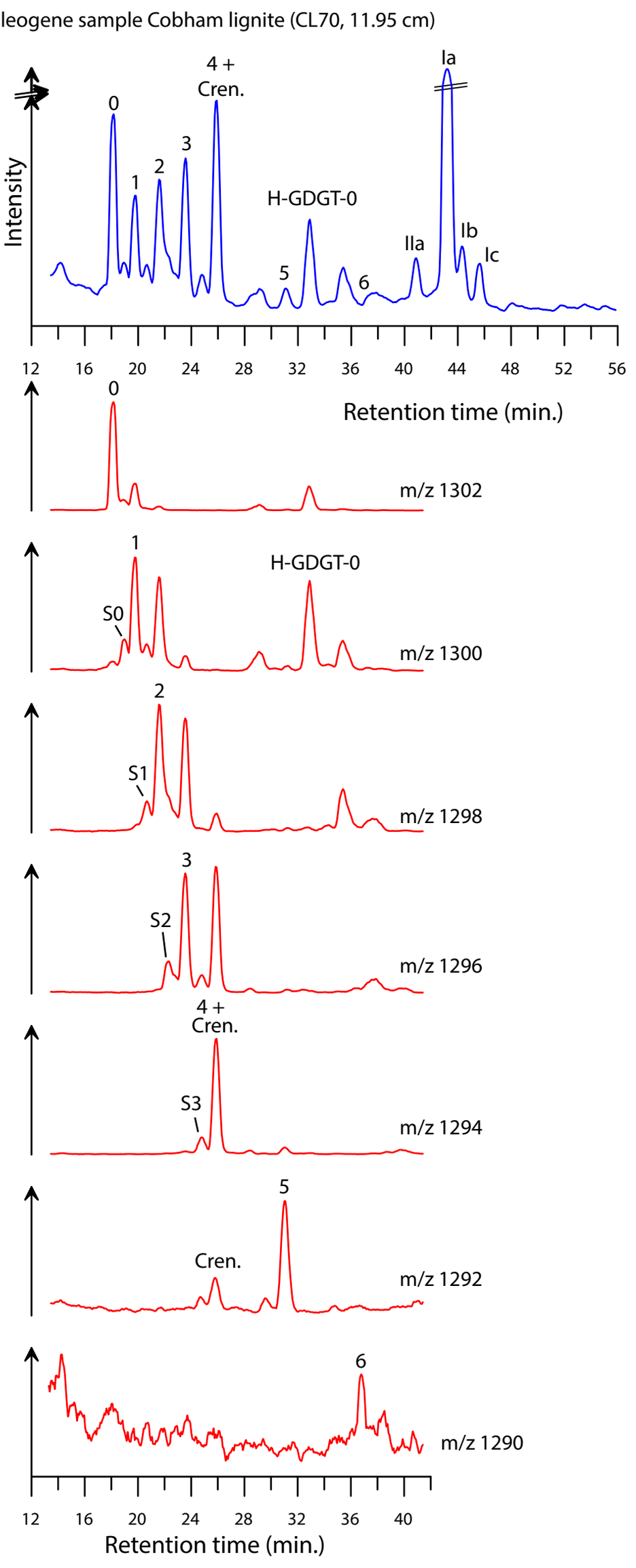
early Paleogene sample Cobham lignite (CL70, 11.95 cm)
Intensity
0
1
2
3
4 +
Cren.
H-GDGT-0
5
6
IIa
Ia
Ib
Ic
12
16
20
24
28
32
36
40
44
48
52
56
Retention time (min.)
m/z 1302
m/z 1300
S0
m/z 1298
S1
m/z 1296
S2
m/z 1294
S3
m/z 1292
Cren.
m/z 1290
Retention time (min.)

Figure S4

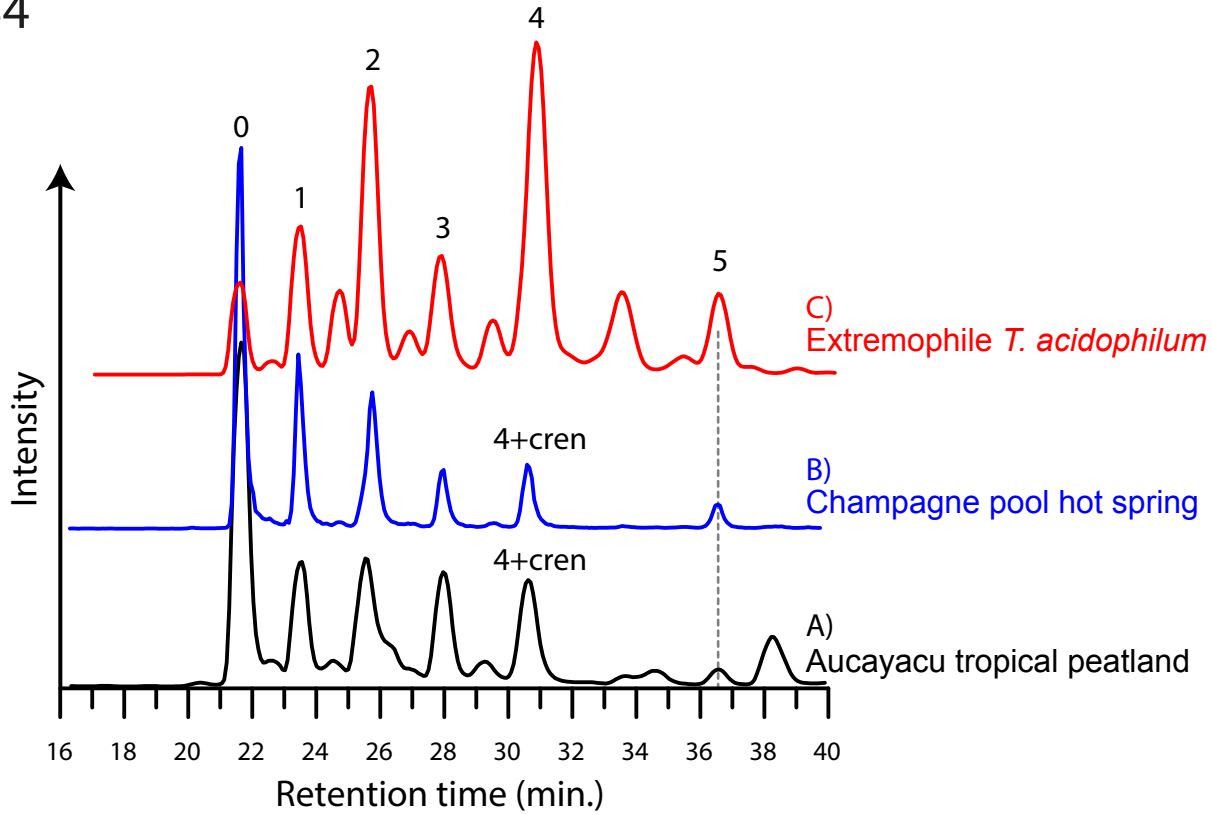
0
1
2
3
4
5
4+cren
4+cren
C)
Extremophile T. acidophilum
B)
Champagne pool hot spring
A)
Aucayacu tropical peatland
Intensity
16
18
20
22
24
26
28
30
32
34
36
38
40
Retention time (min.)

Figure S5

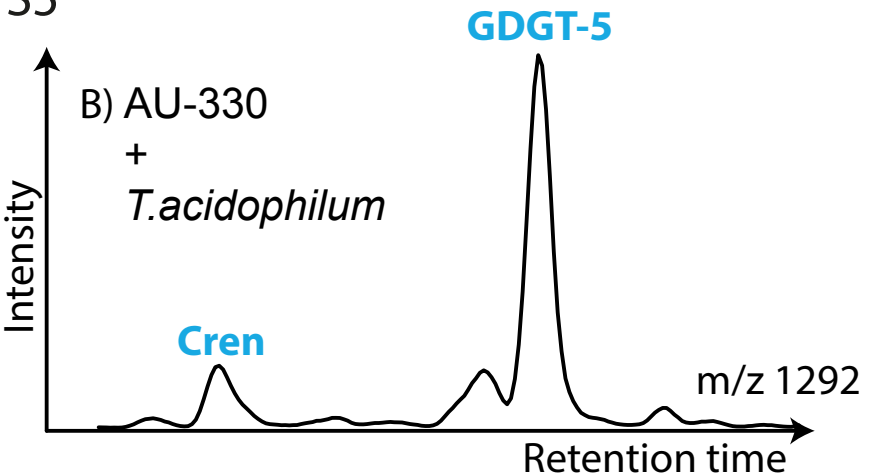
GDGT-5
B) AU-330
+
T.acidophilum
Intensity
Cren
m/z 1292
Retention time

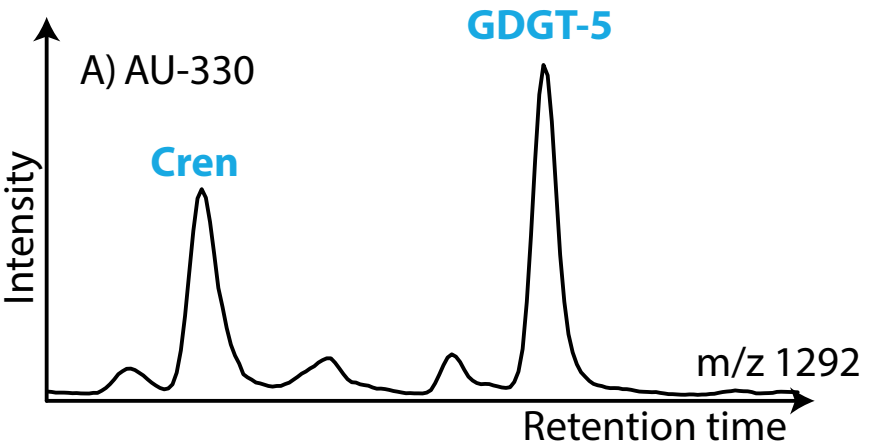
GDGT-5
A) AU-330
Intensity
Cren
m/z 1292
Retention time

Figure S6

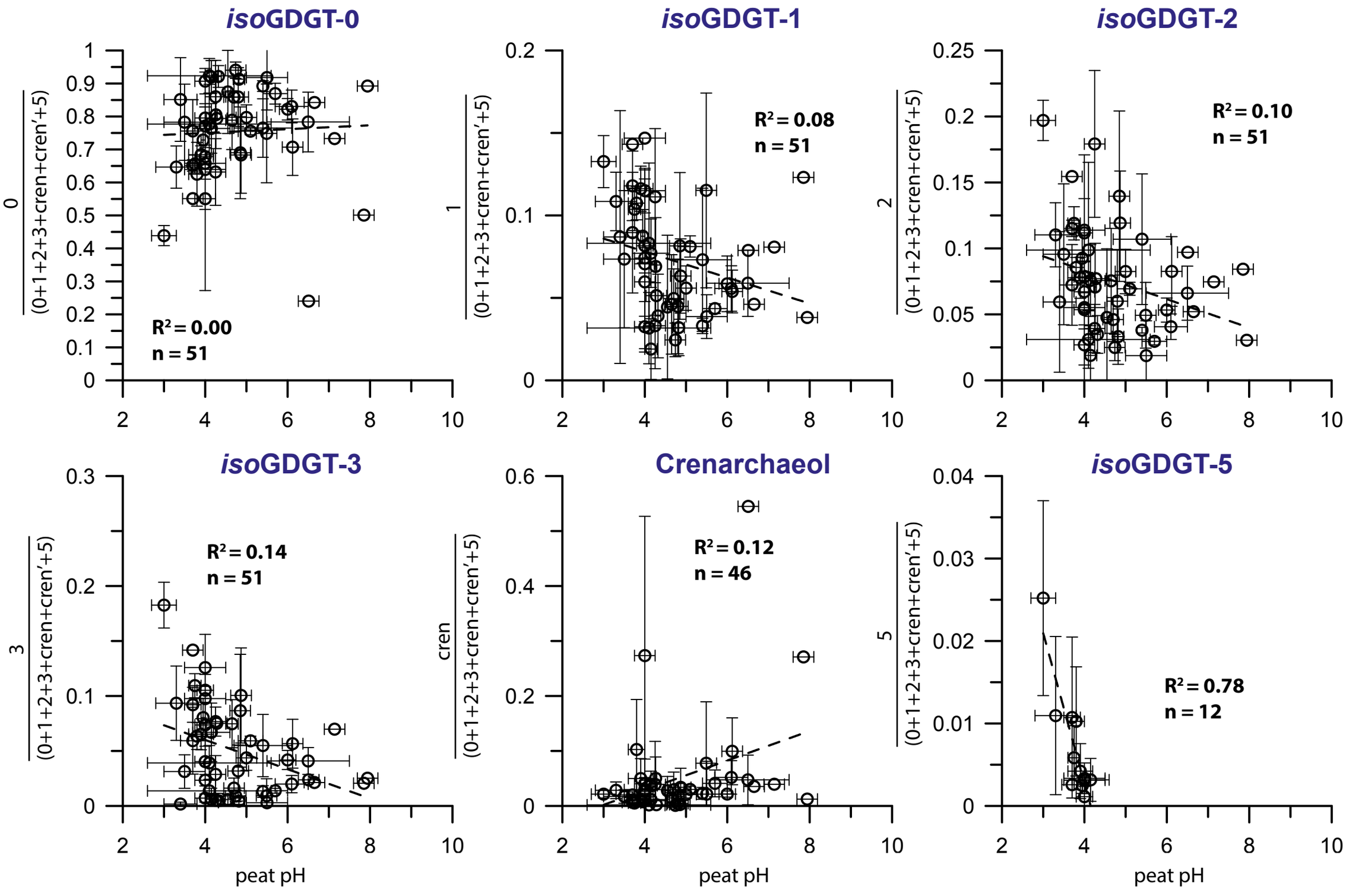
isoGDGT-0
0 / (0+1+2+3+cren+cren'+5)
R² = 0.00
n = 51
isoGDGT-1
1 / (0+1+2+3+cren+cren'+5)
R² = 0.08
n = 51
isoGDGT-2
2 / (0+1+2+3+cren+cren'+5)
R² = 0.10
n = 51
isoGDGT-3
3 / (0+1+2+3+cren+cren'+5)
R² = 0.14
n = 51
Crenarchaeol
cren / (0+1+2+3+cren+cren'+5)
R² = 0.12
n = 46
isoGDGT-5
5 / (0+1+2+3+cren+cren'+5)
R² = 0.78
n = 12
peat pH
peat pH
peat pH

Figure S7

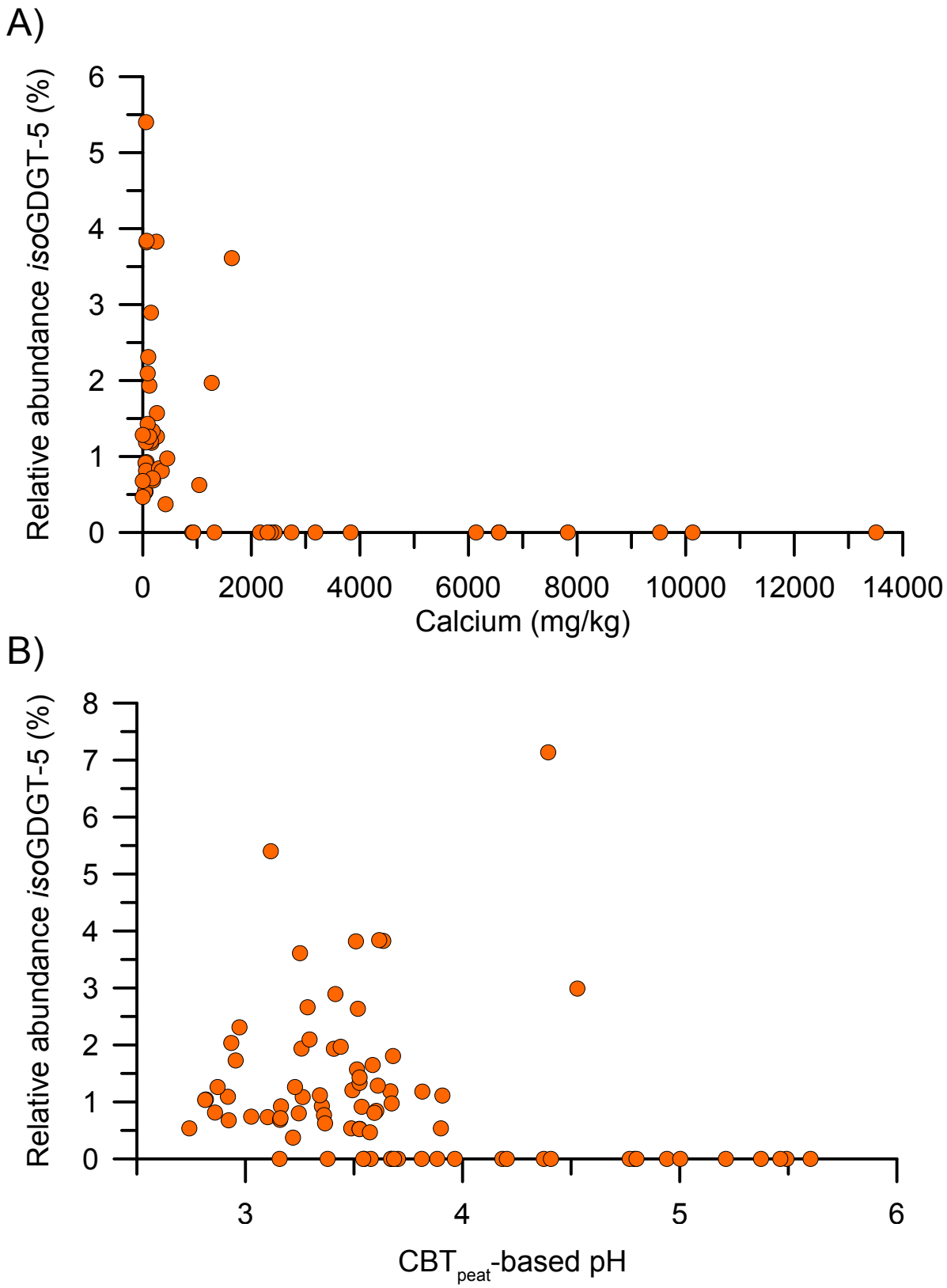
A)
Relative abundance isoGDGT-5 (%)
0
1
2
3
4
5
6
0
2000
4000
6000
8000
10000
12000
14000
Calcium (mg/kg)
B)
Relative abundance isoGDGT-5 (%)
0
1
2
3
4
5
6
7
8
3
4
5
6
CBT peat -based pH

Figure S8

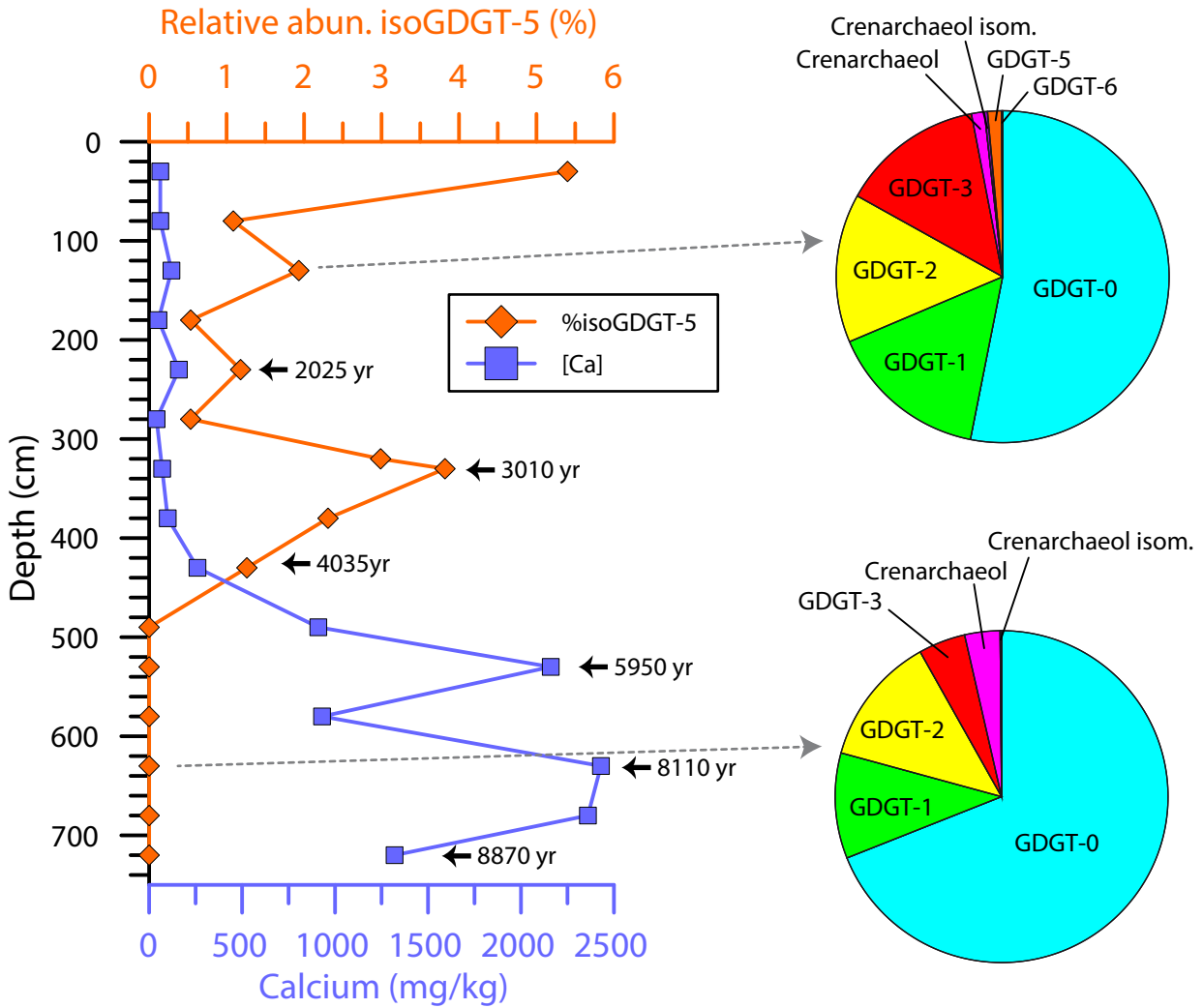
Relative abun. isoGDGT-5 (%)
0
1
2
3
4
5
6
Depth (cm)
0
100
200
300
400
500
600
700
%isoGDGT-5
[Ca]
2025 yr
3010 yr
4035yr
5950 yr
8110 yr
8870 yr
0
500
1000
1500
2000
2500
Calcium (mg/kg)
Crenarchaeol isom.
Crenarchaeol
GDGT-5
GDGT-6
GDGT-3
GDGT-2
GDGT-0
GDGT-1
Crenarchaeol isom.
Crenarchaeol
GDGT-3
GDGT-2
GDGT-1
GDGT-0

Figure S9

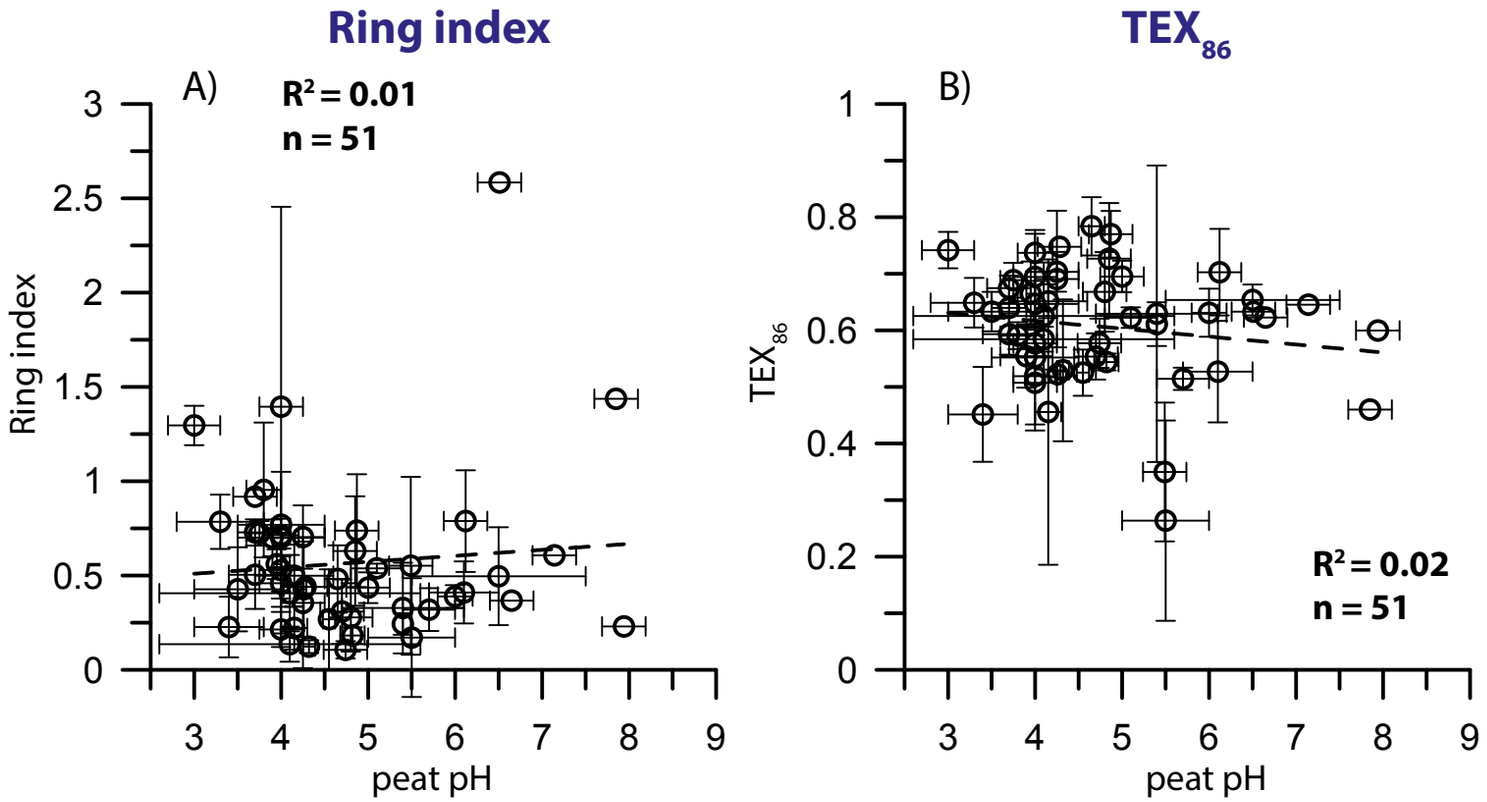
Ring index
A)
R² = 0.01
n = 51
Ring index
peat pH
TEX86
B)
TEX86
peat pH
R² = 0.02
n = 51

Figure S10

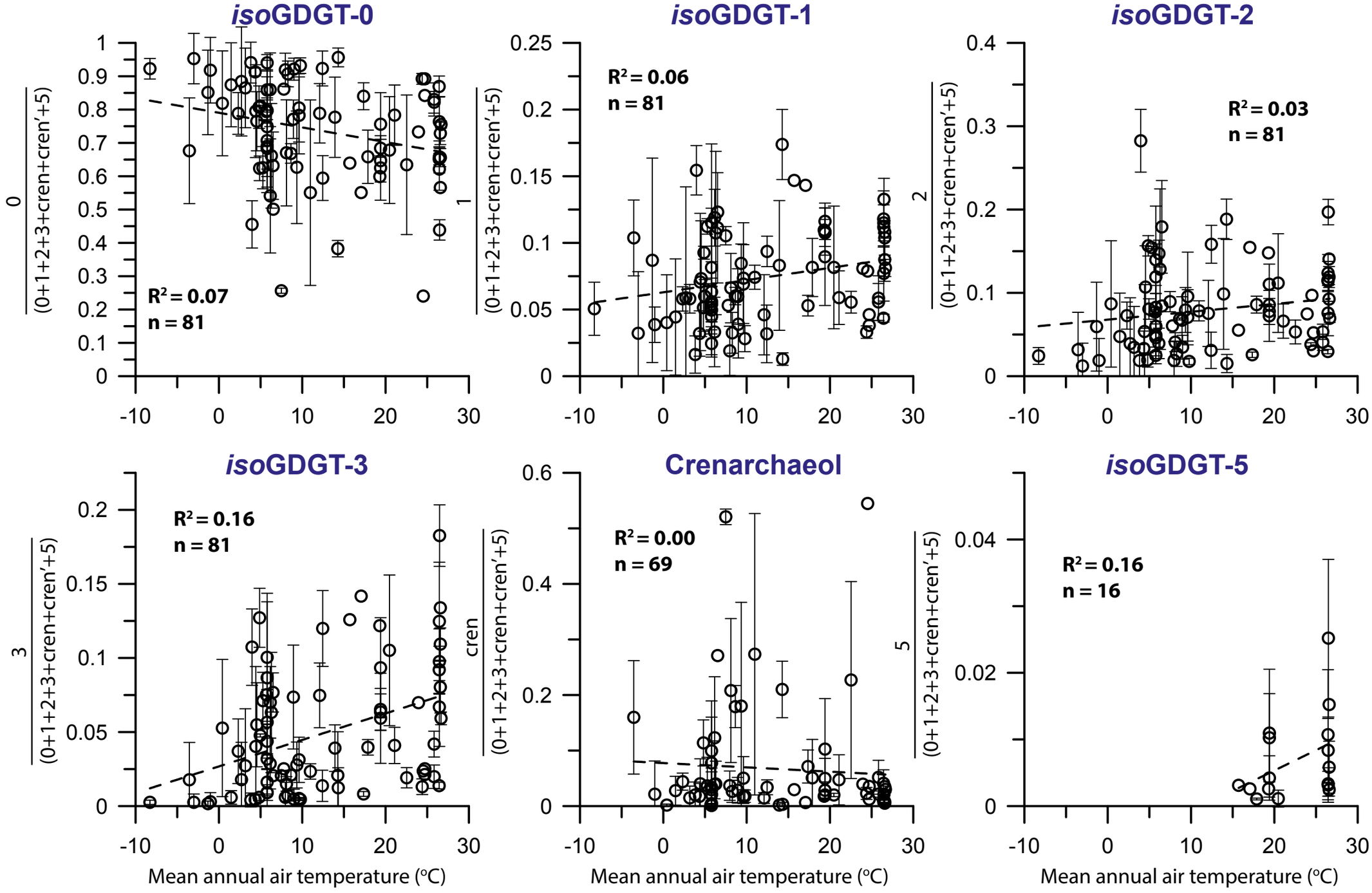
isoGDGT-0
isoGDGT-1
isoGDGT-2
isoGDGT-3
Crenarchaeol
isoGDGT-5
R² = 0.07
n = 81
R² = 0.06
n = 81
R² = 0.03
n = 81
R² = 0.16
n = 81
R² = 0.00
n = 69
R² = 0.16
n = 16
0 (0+1+2+3+cren+cren'+5)
1 (0+1+2+3+cren+cren'+5)
2 (0+1+2+3+cren+cren'+5)
3 (0+1+2+3+cren+cren'+5)
cren (0+1+2+3+cren+cren'+5)
5 (0+1+2+3+cren+cren'+5)
Mean annual air temperature (°C)
Mean annual air temperature (°C)
Mean annual air temperature (°C)

Figure S11

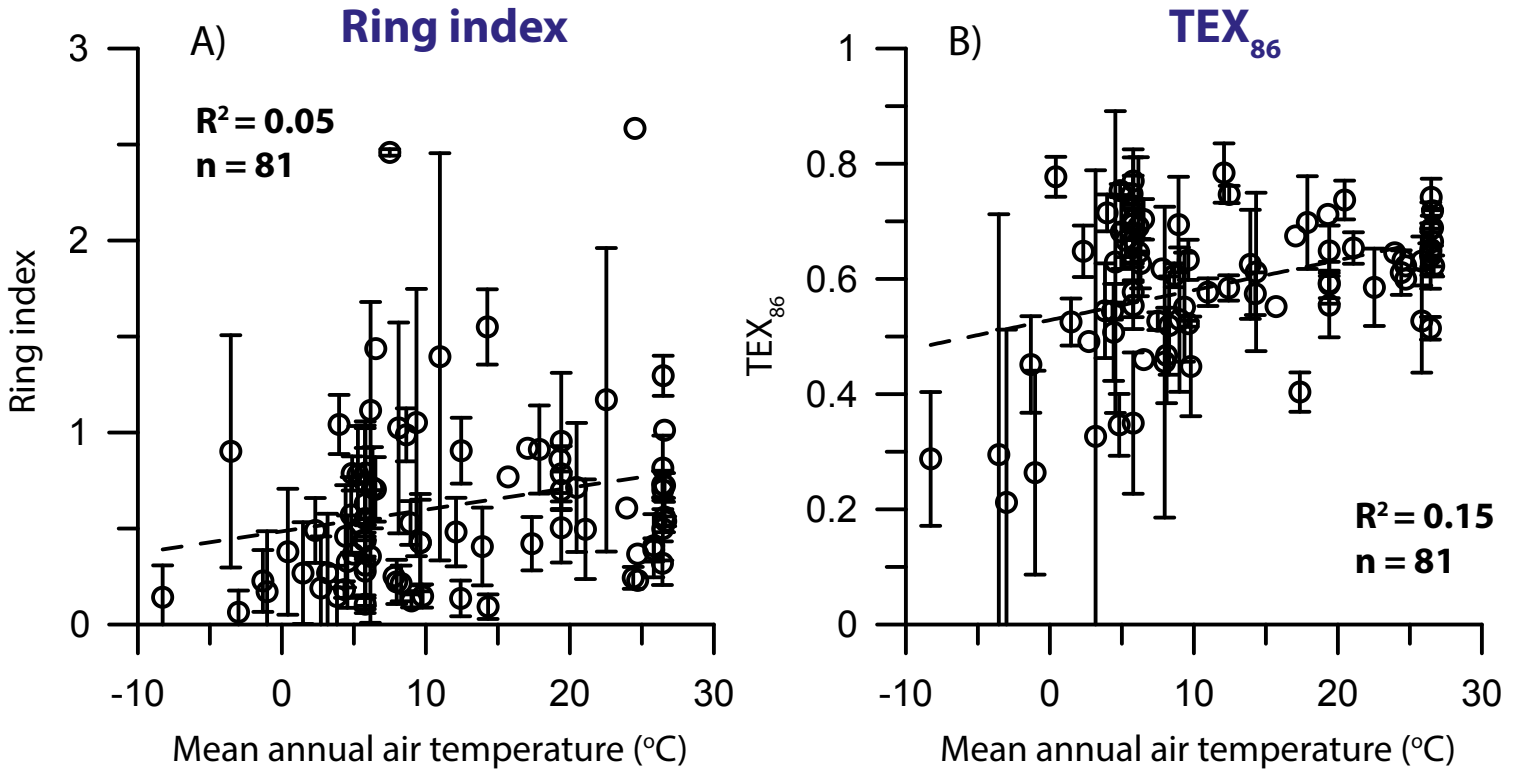
A)
Ring index
$R^2 = 0.05$
n = 81
Ring index
Mean annual air temperature (°C)
B)
TEX_{86}
$R^2 = 0.15$
n = 81
TEX_{86}
Mean annual air temperature (°C)

Figure S12

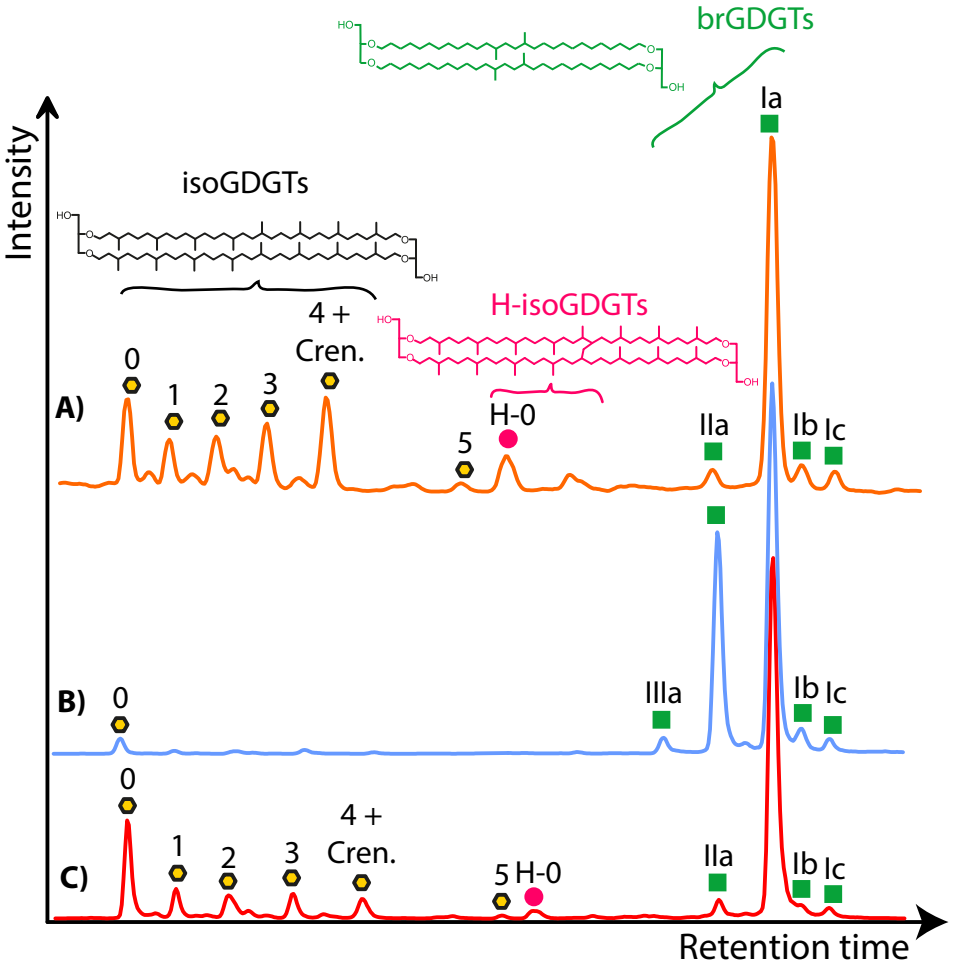
brGDGTs
Ia
isoGDGTs
4 +
Cren.
H-isoGDGTs
Intensity
A)
0
1
2
3
5
H-0
IIa
Ib
Ic
B)
0
IIIa
Ib
Ic
C)
0
1
2
3
4 +
Cren.
5
H-0
IIa
Ib
Ic
Retention time

Figure S13

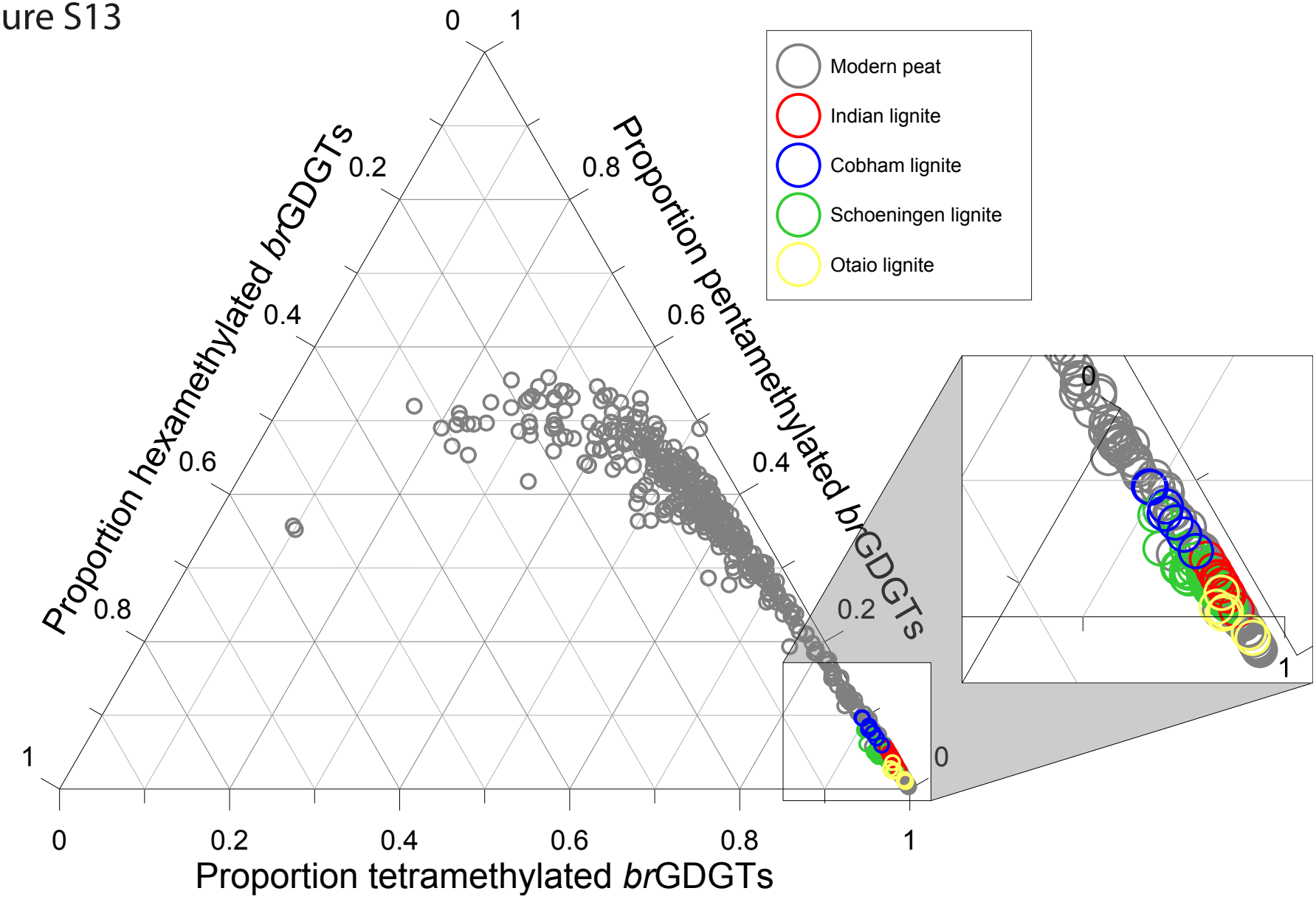
Modern peat
Indian lignite
Cobham lignite
Schoeningen lignite
Otaio lignite
Proportion hexamethylated brGDGTs
Proportion pentamethylated brGDGTs
Proportion tetramethylated brGDGTs
0
0.2
0.4
0.6
0.8
1

Figure S14

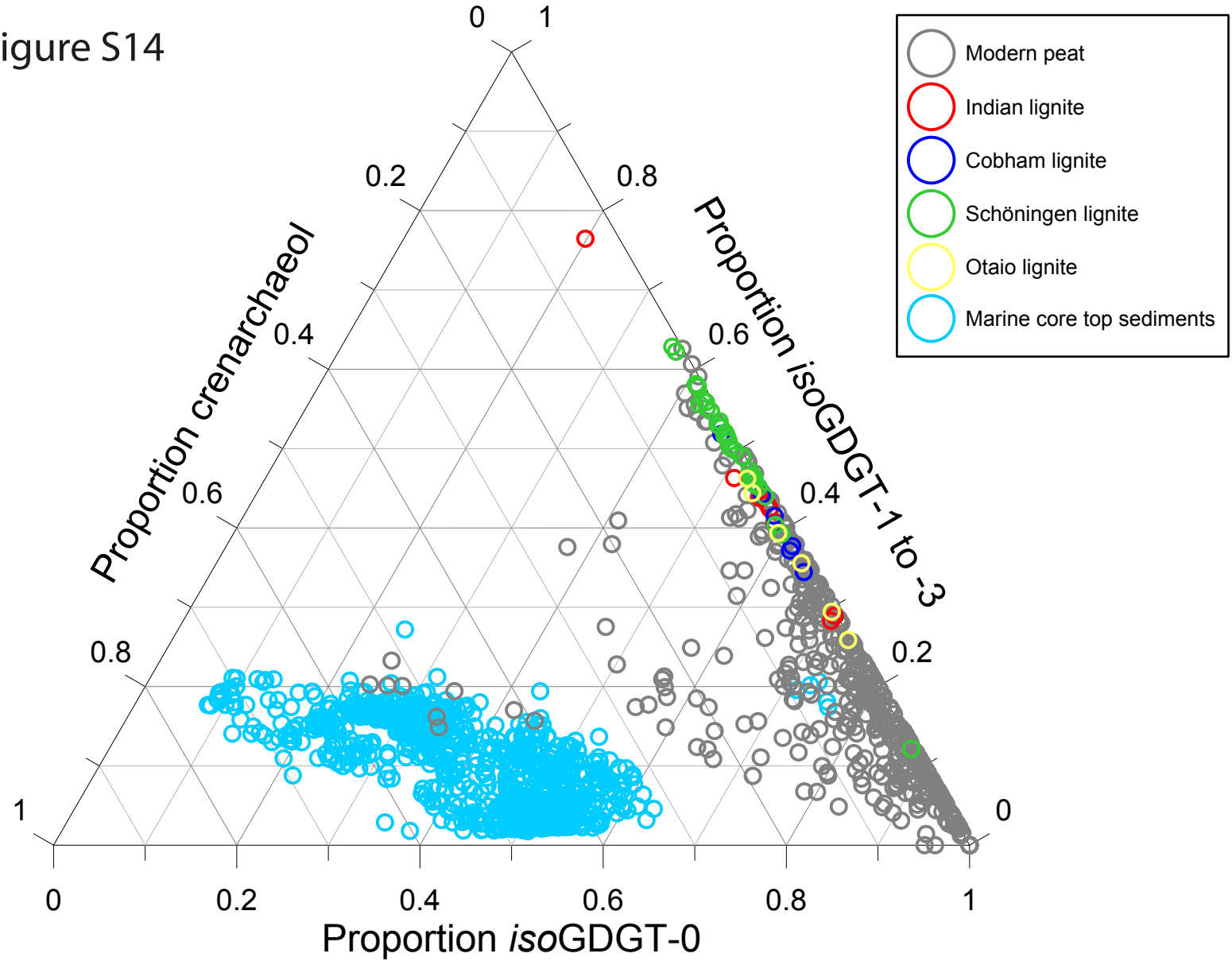
Modern peat
Indian lignite
Cobham lignite
Schöningen lignite
Otaio lignite
Marine core top sediments
Proportion crenarchaeol
Proportion isoGDGT-1 to -3
Proportion isoGDGT-0
0
0.2
0.4
0.6
0.8
1

Figure S15

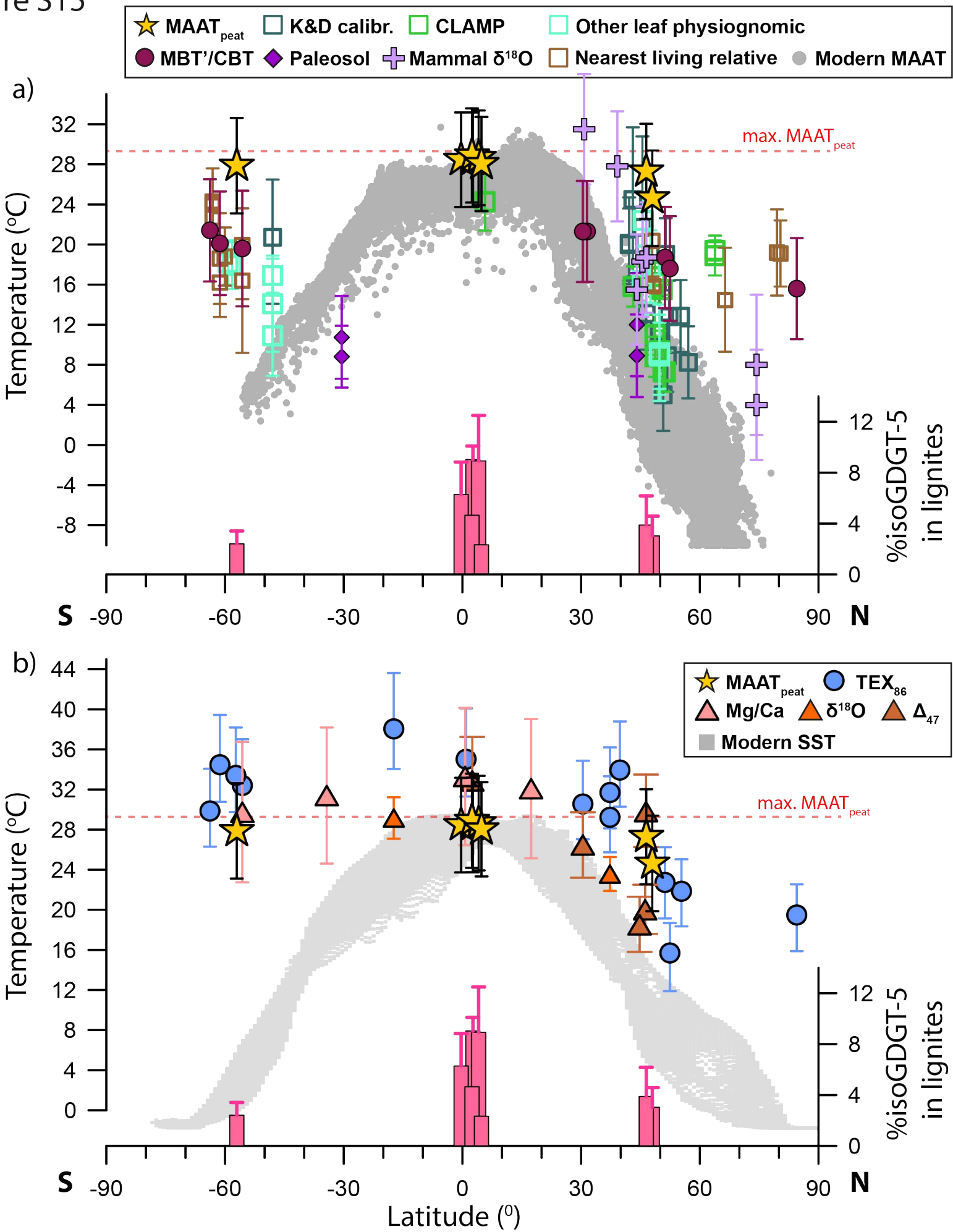
MAAT peat
K&D calibr.
CLAMP
Other leaf physiognomic
MBT'/CBT
Paleosol
Mammal δ18O
Nearest living relative
Modern MAAT
a)
max. MAAT peat
Temperature (°C)
%isoGDGT-5 in lignites
S
N
b)
TEX86
Mg/Ca
δ18O
Δ47
Modern SST
Latitude (°)

Figure S16

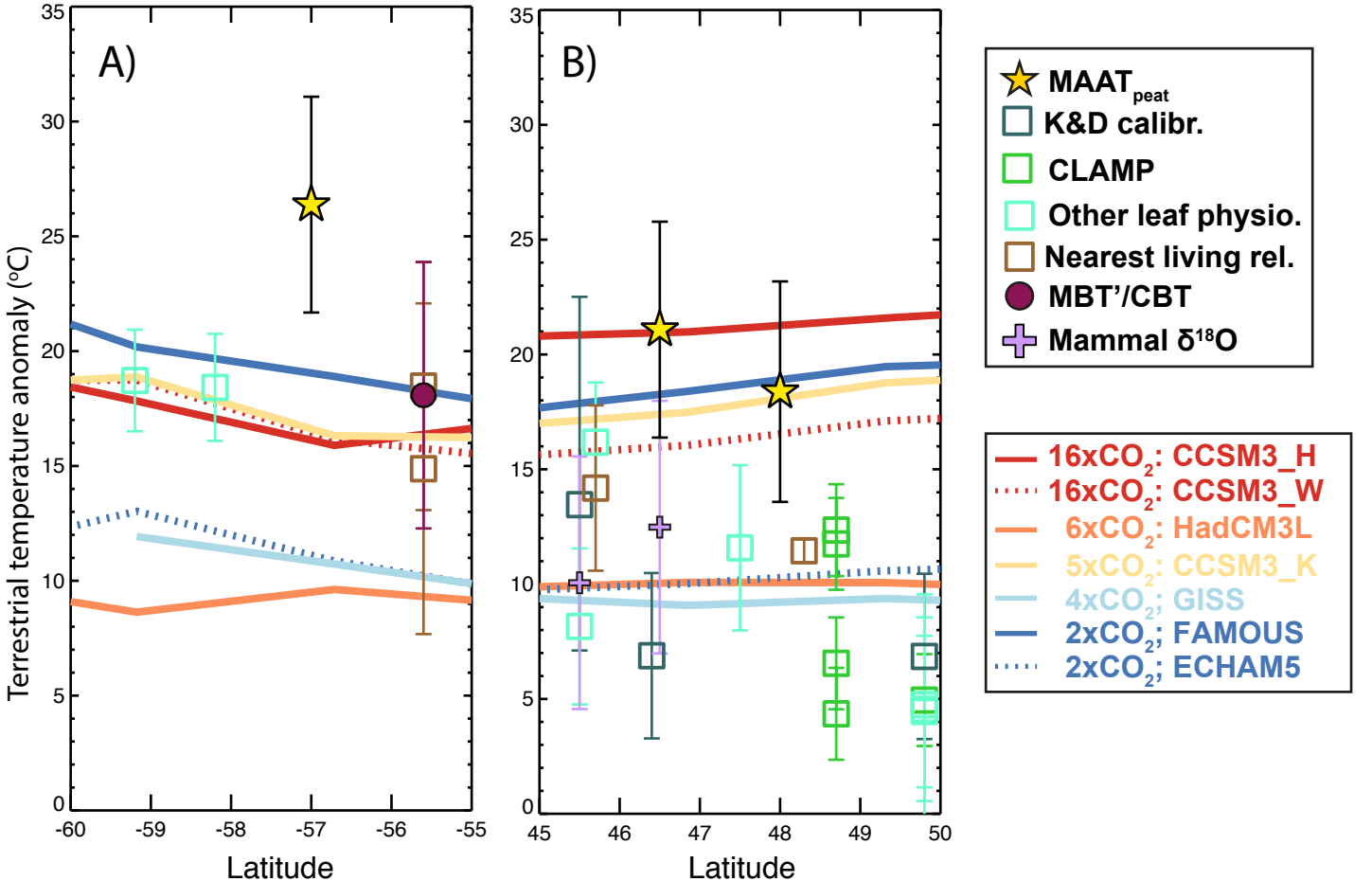
A)
B)
Terrestrial temperature anomaly (°C)
Latitude
Latitude
MAAT peat
K&D calibr.
CLAMP
Other leaf physio.
Nearest living rel.
MBT'/CBT
Mammal δ18O
16xCO2: CCSM3_H
16xCO2: CCSM3_W
6xCO2: HadCM3L
5xCO2: CCSM3_K
4xCO2; GISS
2xCO2; FAMOUS
2xCO2; ECHAM5

Figure S17

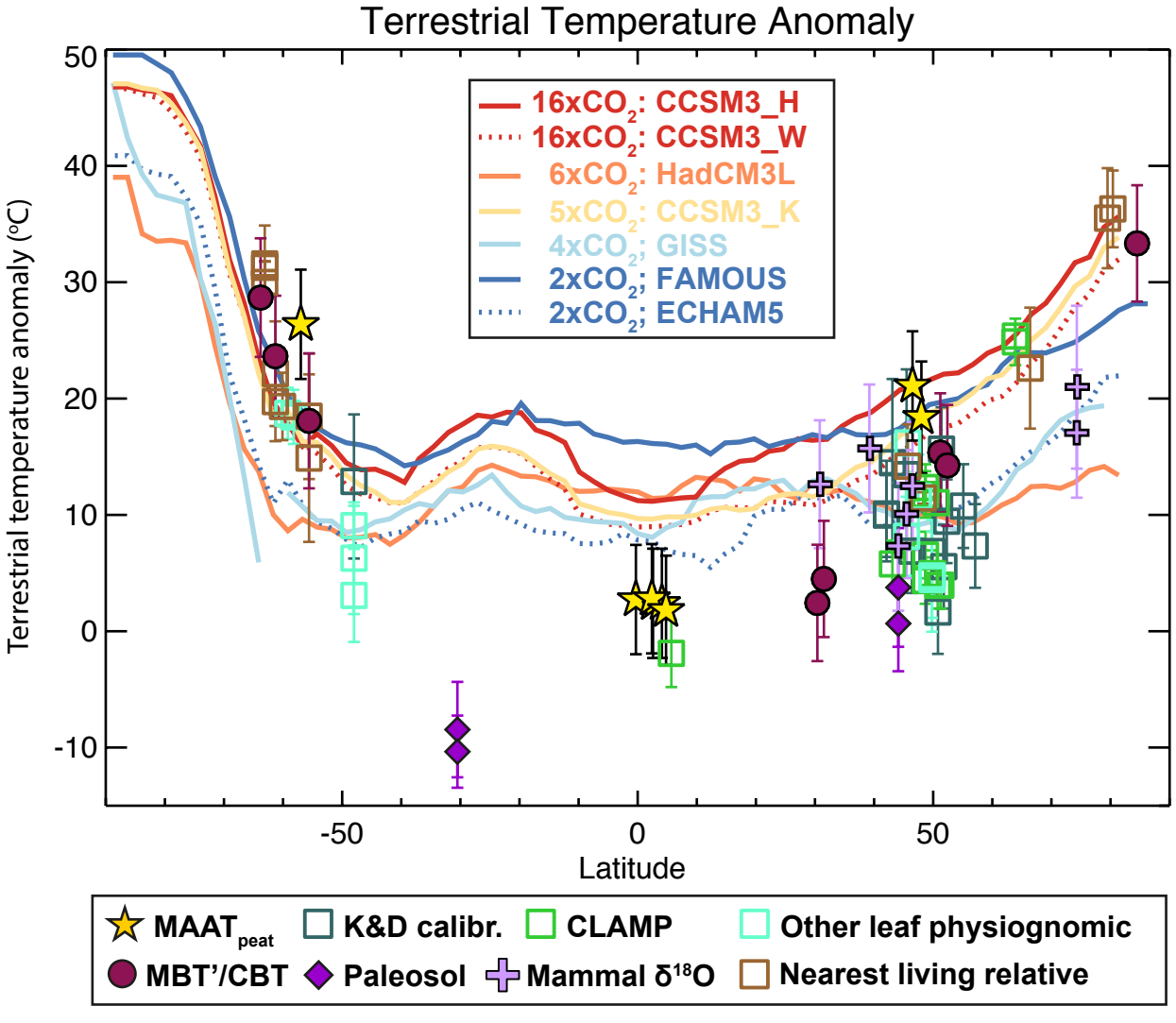
Terrestrial Temperature Anomaly
16xCO2: CCSM3_H
16xCO2: CCSM3_W
6xCO2: HadCM3L
5xCO2: CCSM3_K
4xCO2; GISS
2xCO2; FAMOUS
2xCO2; ECHAM5
Terrestrial temperature anomaly (°C)
50
40
30
20
10
0
-10
-50
0
50
Latitude
MAAT peat
K&D calibr.
CLAMP
Other leaf physiognomic
MBT'/CBT
Paleosol
Mammal δ18O
Nearest living relative